



Centrifugal instability of Taylor–Couette flow in stratified and diffusive fluids

Junho Park 

Centre for Fluid and Complex Systems, Coventry University, Coventry CV1 5FB, UK

Corresponding author: Junho Park, junho.park@coventry.ac.uk

(Received 23 September 2024; revised 2 March 2025; accepted 3 March 2025)

The linear and nonlinear dynamics of centrifugal instability in Taylor–Couette flow are investigated when fluids are stably stratified and highly diffusive. One-dimensional local linear stability analysis (LSA) of cylindrical Couette flow confirms that the stabilising role of stratification in centrifugal instability is suppressed by strong thermal diffusion (i.e. low Prandtl number Pr). For $Pr \ll 1$, it is verified that the instability dependence on thermal diffusion and stratification with the non-dimensional Brunt–Väisälä frequency N can be prescribed by a single rescaled parameter $P_N = N^2 Pr$. From direct numerical simulation (DNS), various nonlinear features such as axisymmetric Taylor vortices at saturation, secondary instability leading to non-axisymmetric patterns or transition to chaotic states are investigated for various values of $Pr \leq 1$ and Reynolds number Re_i . Two-dimensional bi-global LSA of axisymmetric Taylor vortices, which appear as primary centrifugal instability saturates nonlinearly, is also performed to find the secondary critical Reynolds number $Re_{i,2}$ at which the Taylor vortices become unstable by non-axisymmetric perturbation. The bi-global LSA reveals that $Re_{i,2}$ increases (i.e. the onset of secondary instability is delayed) in the range $10^{-3} < Pr < 1$ at $N = 1$ or as N increases at $Pr = 0.01$. Secondary instability leading to highly non-axisymmetric or irregular chaotic patterns is further investigated by three-dimensional DNS. The Nusselt number Nu is also computed from the torque at the inner cylinder for various Pr and Re_i at $N = 1$ to describe how the angular momentum transfer increases with Re_i and how Nu varies differently for saturated and chaotic states.

Key words: Taylor–Couette flow, stratified flows

1. Introduction

Thermal diffusion in fluid flows is characterised by the (thermal) Prandtl number $Pr = \nu_0/\kappa_0$, which denotes the ratio between kinematic viscosity ν_0 and thermal diffusivity κ_0 . The Prandtl number Pr varies from fluid to fluid; for instance, we typically consider $Pr \sim O(10^3)$ for glycerol, $Pr \simeq 7$ for water, $Pr \simeq 0.7$ for air, $Pr \sim O(10^{-1})$ in the Earth's liquid outer core, $Pr \sim O(10^{-2})$ for liquid metals, $Pr \sim O(10^{-6})$ or less in the interior of the Sun and stars (Calkins *et al.* 2012; Horn *et al.* 2013; Garaud 2020a; Legaspi & Waite 2020). The Prandtl-number dependence has been examined for various flows coupled with heat transfer. In convection, Kerr & Herring (2000) studied a thermal convection problem with no-slip vertical boundaries and free-slip lateral boundaries and they proposed different scaling laws for the Nusselt number Nu versus the Rayleigh number Ra transitions as $Nu \sim Ra^{2/7}$ for $Pr \sim O(1)$ and $Nu \sim Ra^{1/4}$ for low $Pr \ll 1$. Miquel *et al.* (2020) investigated the convection in a different configuration with internal sources and sinks and they proposed a different scaling law as $Nu \sim Ra^{1/2} Pr^\chi$, where the exponent χ transitions from $\chi \simeq 1/2$ for $Pr \leq 0.04$ to $\chi \simeq 1/6$ for $Pr > 0.04$. The Prandtl-number dependence has also been explored in studies of stratified flows. For instance, it is found that turbulence in stably stratified fluids permits high-wavenumber temperature fluctuation that leads to the appearance of small-scale turbulence structures as Pr increases when $Pr > 1$ (Legaspi & Waite 2020). The effect of thermal diffusion is examined in a study of exact coherent structures in stratified plane Couette flow in the limits of either $Pr \rightarrow 0$ or $Pr \rightarrow \infty$, the former in which the thermal diffusion is dominant over stratification and the density variation away from a linear profile of the stratification vanishes and the latter in which the density can be mixed and homogenised by advection and its stratification profile deviates from a linear profile (Langham *et al.* 2020).

Fluid flows with stratification and strong thermal diffusion with $Pr \ll 1$ have been the subject of interest in geophysics and astrophysics due to their relevance to the interior of the Earth and stars including the Sun (Lignières 1999; Calkins *et al.* 2012; Garaud 2020a). Figure 1 illustrates a configuration in which a fluid parcel is hypothetically displaced upwards over a length scale L_0 in a stably stratified fluid with the temperature gradient along the vertical direction of gravity. The temperature of the parcel is lower than the surrounding temperature so the parcel absorbs heat at a rate with a characteristic diffusion time scale $\tau_{diff} = L_0^2/\kappa_0$. Simultaneously, the stratification acts as a restoring force on the parcel leading to internal oscillation with a period $\tau_{int} = 1/N_0$, where N_0 is the dimensional Brunt–Väisälä frequency derived from the stratification. On the one hand, if the thermal diffusivity is low as $\kappa_0 \ll N_0 L_0^2$ (i.e. the diffusion time scale is much larger than the internal oscillation period as $\tau_{diff} \gg \tau_{int}$), the restoring force is dominant and the fluid parcel descends to the original position due to the gravitational force, a well-known mechanism for the generation of internal gravity waves. On the other hand, if the thermal diffusivity is high as $\kappa_0 \gg N_0 L_0^2$ (i.e. $\tau_{diff} \ll \tau_{int}$), the gravitational force will be weakened due to the rapidly increased temperature of the fluid parcel. In this case, the parcel descends and stops at a position higher than the original position (figure 1a). This implies that strong thermal diffusion can suppress the internal oscillation and the effect of stratification suppressing the vertical fluid motion becomes weak as a consequence.

Such a stratification effect affected by strong thermal diffusion has been considered in prescribing shear instability-driven turbulence and associated angular momentum transport in stellar radiation zones where fluids are stably stratified and the Prandtl number Pr is low. For instance, for low Péclet number $Pe = RePr$, where Re is the Reynolds number, Lignières (1999) proposed a small-Péclet-number approximation that provides an asymptotic form of the Boussinesq equations in the small- Pe limit where

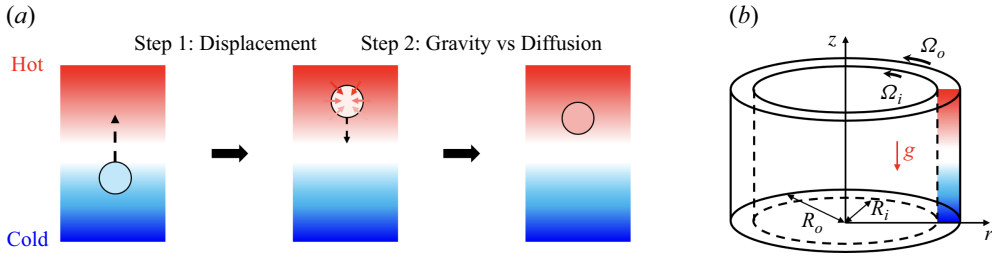


Figure 1. (a) Illustration of how the internal oscillation of a fluid parcel in stably stratified fluid is suppressed by a fast thermal diffusion process. (b) Schematic of Taylor–Couette flow with stable temperature stratification.

thermal diffusion and stratification can be combined and described as a single physical process. For vertical shear instability in stratified and highly diffusive fluids, Lignières *et al.* (1999) revealed that instability characteristics for various N_0 and $Pr \ll 1$ can be expressed in terms of a single rescaled number $R_P = Ri Pe$, where $Ri = N_0^2/S_0^2$ is the Richardson number with a characteristic shear S_0 . Instead of the classical Richardson number criterion for shear instability in stratified flow, $Ri < 1/4$, the modified Richardson number criterion $R_P < O(1)$ is adopted in the prescription of turbulent effective viscosity in the low- Pe limit for simulations of the evolution of stars (e.g. Zahn 1992; Mathis *et al.* 2018; Prat & Mathis 2021). For horizontal shear flows in stratified-rotating fluids, Park *et al.* (2020, 2021b) reported similar dynamical behaviours such as the stratification effect suppressed by high thermal diffusivity or instability characteristics described by the rescaled parameter R_P for shear instabilities in the low- Pe limit. The small-Péclet-number approximation with the rescaled parameter R_P is also used in turbulence simulations of horizontal and vertical shear flows in stratified and highly diffusive fluids (Prat & Lignières 2013, 2014) and more attention has been paid recently to the low- Pr and low- Pe regimes in stratified turbulence (Cope *et al.* 2020; Garaud 2020a; Chang & Garaud 2021; Garaud *et al.* 2024b). It is noteworthy that Péclet numbers of actual astrophysical systems are too high (e.g. $Pe \sim O(10^7)$ with $Re \sim O(10^{13})$ and $Pr \sim O(10^{-6})$ for the solar tachocline; see also Garaud 2020b) and fully resolved astrophysical turbulence for such high Re and Pe is not achievable yet from any state-of-the-art simulations. The current study also cannot address high- Re /high- Pe turbulence but still aims to explain the role of strong thermal diffusion at low Pr .

Despite the increasing interest in the effect of strong thermal diffusion on stratified shear flows, the Prandtl-number dependence has not been studied considerably in the context of Taylor–Couette flow, a canonical shear flow between two concentric cylinders rotating independently, in a stably stratified fluid (figure 1b). Stratification in Taylor–Couette flow tends to suppress the vertical fluid motion and, as a result, the onset of centrifugal instability is delayed and the vertical length scale of axisymmetric Taylor vortices is reduced as the stratification becomes strong (Withjack & Chen 1975; Boubnov *et al.* 1995; Caton *et al.* 2000). An interesting phenomenon in stratified Taylor–Couette flow is non-axisymmetric strato-rotational instability (SRI), which occurs due to the resonance between inertia–gravity waves confined between the two cylinders (Molemaker *et al.* 2001; Yavneh *et al.* 2001). The SRI has been explored extensively by theoretical investigations (e.g. Rüdiger & Shalybkov 2009; Le Dizès & Riedinger 2010; Park & Billant 2013; Leclercq *et al.* 2016; Wang & Balmforth 2018; Robins *et al.* 2020), experiments (e.g. Le Bars & Le Gal 2007; Ibanez *et al.* 2016; Rüdiger *et al.* 2017; Park *et al.* 2018; Seelig *et al.* 2018) and numerical simulations (e.g. Lopez & Marques 2020; Meletti *et al.* 2021; Lopez & Marques 2022). These instability studies considered the Prandtl number of $O(1)$

for fluids like water or air or simply $Pr = \infty$ to neglect the effect of thermal diffusion in theoretical analyses, or they considered the analogous Schmidt number $Sc = \nu_0/D_0$ (where D_0 is a diffusivity of scalars like density, salinity, etc.) of $O(100)$ if stratification of water by salt is considered in experiments. Investigating the dynamics of stratified Taylor–Couette flow under the influence of thermal diffusion, in particular in the low- Pr limit, is important as the results can further be used to provide insights into large-scale flows and propose turbulent viscosity models in multi-physics simulations of astrophysical and geophysical systems such as simulations of the evolution of stars (Richard & Zahn 1999; Dubrulle *et al.* 2005). However, Taylor–Couette flow in stratified and highly diffusive fluids is still poorly understood and this motivates our study of stratified Taylor–Couette flow and firstly its centrifugal instability under the influence of strong thermal diffusion at low Prandtl number $Pr \leq 1$.

The paper consists of the following sections to investigate the centrifugal instability of Taylor–Couette flow in stratified and diffusive fluids. In § 2, the problem formulation and details of numerical methods are provided. In § 3, one-dimensional (1-D) local linear stability analysis (LSA) is performed to present LSA results on centrifugal instability of cylindrical Couette flow for various parameters. In § 4, two-dimensional (2-D) and three-dimensional (3-D) direct numerical simulations (DNS) are conducted to investigate the nonlinear dynamics of centrifugal instability such as saturation, secondary instability or transition to chaotic states. In § 5, conclusion and discussion are provided.

2. Problem formulation and methodology

2.1. Navier–Stokes equations under the Boussinesq approximation

In this study, we consider the Boussinesq approximation in which the reference density ρ_0 is assumed to be much larger than the density variation ϱ (i.e. $\rho_0 \gg \varrho$). The density variation ϱ is assumed to satisfy a linear relation with the total temperature ϑ as $\varrho/\rho_0 = -\alpha_0(\vartheta - \vartheta_0)$ where $\alpha_0 > 0$ is the thermal expansion coefficient and ϑ_0 is the reference temperature. For velocity $\mathbf{U} = (U_r, U_\theta, U_z)$, temperature variation $\Theta = \vartheta - \vartheta_0$ and associated pressure variation P in cylindrical coordinates (r, θ, z) , we consider the following continuity, momentum and energy equations:

$$\nabla \cdot \mathbf{U} = 0, \quad (2.1)$$

$$\frac{\partial \mathbf{U}}{\partial t} + \mathbf{U} \cdot \nabla \mathbf{U} = -\frac{1}{\rho_0} \nabla P + \alpha_0 g \Theta \vec{e}_z + \nu_0 \nabla^2 \mathbf{U}, \quad (2.2)$$

$$\frac{\partial \Theta}{\partial t} + \mathbf{U} \cdot \nabla \Theta = \kappa_0 \nabla^2 \Theta, \quad (2.3)$$

where g is the gravitational acceleration in the vertical direction z , ν_0 is the kinematic viscosity, κ_0 is the thermal diffusivity and ∇^2 is the Laplacian operator. We consider cylindrical Couette flow in a stably stratified fluid as a base state with base velocity $\mathbf{U}_B = (0, V_B(r), 0)$ and base temperature $T_B(z)$ as

$$V_B(r) = Ar + \frac{B}{r}, \quad A = \Omega_i \frac{\mu - \eta^2}{1 - \eta^2}, \quad B = \Omega_i R_i^2 \frac{1 - \mu}{1 - \eta^2}, \quad T_B(z) = \frac{\Delta T}{\Delta z} z, \quad (2.4)$$

where $V_B(r)$ is the base azimuthal velocity, A and B are constants as a function of the angular velocities Ω_i and Ω_o and radii R_i and R_o (where the subscripts i and o denote the inner and outer cylinders, respectively), $\mu = \Omega_o/\Omega_i$ is the angular velocity ratio,

$\eta = R_i/R_o$ is the radius ratio and ΔT is the temperature difference along the vertical distance Δz . Throughout this paper, we consider only the case in which the outer cylinder is fixed and only the inner cylinder rotates (i.e. $\Omega_o = 0$ and $\mu = 0$). The temperature gradient $\Delta T/\Delta z$ is assumed to be positive and constant so the fluid is stably stratified and the base temperature T_B increases linearly with z . The base pressure $P_B(r, z)$ balances the velocity V_B and temperature T_B by satisfying the following relations:

$$-\frac{V_B^2}{r} = -\frac{1}{\rho_0} \frac{\partial P_B}{\partial r}, \quad 0 = -\frac{1}{\rho_0} \frac{\partial P_B}{\partial z} + \alpha_0 g T_B. \quad (2.5)$$

Equations (2.1)–(2.3) can be expressed in a non-dimensional form by considering R_i as the reference length, Ω_i^{-1} as the reference time, $R_i \Omega_i$ as the reference velocity, $\rho_0 R_i^2 \Omega_i^2$ as the reference pressure and ΔT as the reference temperature. The distance Δz can be chosen arbitrarily without loss of generality; thus we choose $\Delta z = R_i$ for simplicity. The coordinates z and r are considered non-dimensional hereafter, and hence the base temperature can simply be expressed as $T_B(z) = z$.

We consider perturbation with its velocity $\mathbf{u} = \mathbf{U} - \mathbf{U}_B = (u_r, u_\theta, u_z)$, pressure $p = P - P_B$ and temperature $T = \Theta - T_B$. By applying the base state and perturbation to (2.1)–(2.3) and subtracting the base-state equations (2.4)–(2.5), we obtain the Navier–Stokes equations for perturbation as follows:

$$\frac{\partial u_r}{\partial t} + \frac{u_r}{r} + \frac{1}{r} \frac{\partial u_\theta}{\partial \theta} + \frac{\partial u_z}{\partial z} = 0, \quad (2.6)$$

$$\frac{\partial u_r}{\partial t} + \Omega \frac{\partial u_r}{\partial \theta} - 2\Omega u_\theta + N_r = -\frac{\partial p}{\partial r} + \frac{1}{Re} \left(\nabla^2 u_r - \frac{u_r}{r^2} - \frac{2}{r^2} \frac{\partial u_\theta}{\partial \theta} \right), \quad (2.7)$$

$$\frac{\partial u_\theta}{\partial t} + \Omega \frac{\partial u_\theta}{\partial \theta} + Z u_r + N_\theta = -\frac{1}{r} \frac{\partial p}{\partial \theta} + \frac{1}{Re} \left(\nabla^2 u_\theta - \frac{u_\theta}{r^2} + \frac{2}{r^2} \frac{\partial u_r}{\partial \theta} \right), \quad (2.8)$$

$$\frac{\partial u_z}{\partial t} + \Omega \frac{\partial u_z}{\partial \theta} + N_z = -\frac{\partial p}{\partial z} + N^2 T + \frac{1}{Re} \nabla^2 u_z, \quad (2.9)$$

$$\frac{\partial T}{\partial t} + \Omega \frac{\partial T}{\partial \theta} + u_z + N_T = \frac{1}{Re Pr} \nabla^2 T, \quad (2.10)$$

where $\Omega(r) = V_B/r$ is the base angular velocity, $Z(r) = (1/r)d(r^2\Omega)/dr$ is the base axial vorticity and N_r , N_θ , N_z and N_T are nonlinear terms:

$$N_r = u_r \frac{\partial u_r}{\partial r} + \frac{u_\theta}{r} \frac{\partial u_r}{\partial \theta} + u_z \frac{\partial u_r}{\partial z} - \frac{u_\theta^2}{r}, \quad (2.11)$$

$$N_\theta = u_r \frac{\partial u_\theta}{\partial r} + \frac{u_\theta}{r} \frac{\partial u_\theta}{\partial \theta} + u_z \frac{\partial u_\theta}{\partial z} + \frac{u_r u_\theta}{r}, \quad (2.12)$$

$$N_z = u_r \frac{\partial u_z}{\partial r} + \frac{u_\theta}{r} \frac{\partial u_z}{\partial \theta} + u_z \frac{\partial u_z}{\partial z}, \quad (2.13)$$

$$N_T = u_r \frac{\partial T}{\partial r} + \frac{u_\theta}{r} \frac{\partial T}{\partial \theta} + u_z \frac{\partial T}{\partial z}. \quad (2.14)$$

The parameters Re , N and Pr are the Reynolds number, non-dimensional Brunt–Väisälä frequency and Prandtl number, respectively, which are defined as

$$Re = \frac{R_i^2 \Omega_i}{\nu_0}, \quad N = \sqrt{\frac{\alpha_0 g}{\Omega_i^2} \frac{\Delta T}{\Delta z}}, \quad Pr = \frac{\nu_0}{\kappa_0}. \quad (2.15)$$

For convenience in comparison with other literature, we also use a conventional inner-cylinder-based Reynolds number Re_i defined as

$$Re_i = \frac{R_i \Omega_i d}{\nu_0} = Re \left(\frac{1 - \eta}{\eta} \right), \quad (2.16)$$

where $d = R_o - R_i$ is the gap size between the two cylinders.

2.2. Pseudo-spectral formulation for direct numerical simulation

In this study, spectral-based DNS are conducted to solve (2.6)–(2.10) numerically. To do so, we decompose the perturbation into the sum of modes using the following Fourier representation:

$$\begin{pmatrix} u_r \\ u_\theta \\ u_z \\ T \\ p \end{pmatrix} = \sum_{j=-M}^M \sum_{l=-K}^K \begin{pmatrix} \tilde{u}_{jl}(r, t) \\ \tilde{v}_{jl}(r, t) \\ \tilde{w}_{jl}(r, t) \\ \tilde{T}_{jl}(r, t) \\ \tilde{p}_{jl}(r, t) \end{pmatrix} \exp(im_j \theta + ik_l z), \quad (2.17)$$

where M and K are the cut-off numbers of modes considered in the azimuthal direction θ and axial direction z , respectively, \tilde{u}_{jl} , \tilde{v}_{jl} , \tilde{w}_{jl} , \tilde{p}_{jl} and \tilde{T}_{jl} are the time-dependent mode shapes, $m_j = jm$ is the j th multiple of the principal azimuthal wavenumber m and $k_l = lk$ is the l th multiple of the principal axial wavenumber k . The above ansatz (2.17) is used for various problems such as the Taylor–Couette formulation in *nsCouette* code (López *et al.* 2020) or convection problems (Saltzman 1962; Park *et al.* 2021a). The formulation is also analogous to semi-linear models, which are applied to centrifugal instability of anti-cyclonic vortices (Yim *et al.* 2020, 2023). The semi-linear theory allows us to investigate directly nonlinear interaction between base flow and an instability mode, and the method is generalised by considering nonlinear interaction among multiple instability modes in low-order harmonics while neglecting the triad interaction leading to harmonics of orders higher than the cut-off numbers. For each mode with indices j and l , we apply the ansatz (2.17) to (2.6)–(2.10) and obtain

$$\frac{\partial \tilde{u}_{jl}}{\partial r} + \frac{\tilde{u}_{jl}}{r} + \frac{im_j \tilde{v}_{jl}}{r} + ik_l \tilde{w}_{jl} = 0, \quad (2.18)$$

$$\frac{\partial \tilde{u}_{jl}}{\partial t} + im_j \Omega \tilde{u}_{jl} - 2\Omega \tilde{v}_{jl} + \tilde{N}_{r,jl} = -\frac{\partial \tilde{p}_{jl}}{\partial r} + \frac{1}{Re} \left(\tilde{\nabla}_{jl}^2 \tilde{u}_{jl} - \frac{\tilde{u}_{jl}}{r^2} - \frac{2im_j \tilde{v}_{jl}}{r^2} \right), \quad (2.19)$$

$$\frac{\partial \tilde{v}_{jl}}{\partial t} + im_j \Omega \tilde{v}_{jl} + Z \tilde{u}_{jl} + \tilde{N}_{\theta,jl} = -\frac{im_j \tilde{p}_{jl}}{r} + \frac{1}{Re} \left(\tilde{\nabla}_{jl}^2 \tilde{v}_{jl} - \frac{\tilde{v}_{jl}}{r^2} + \frac{2im_j \tilde{u}_{jl}}{r^2} \right), \quad (2.20)$$

$$\frac{\partial \tilde{w}_{jl}}{\partial t} + im_j \Omega \tilde{w}_{jl} + \tilde{N}_{z,jl} = -ik_l \tilde{p}_{jl} + N^2 \tilde{T}_{jl} + \frac{1}{Re} \tilde{\nabla}_{jl}^2 \tilde{w}_{jl}, \quad (2.21)$$

$$\frac{\partial \tilde{T}_{jl}}{\partial t} + im_j \Omega \tilde{T}_{jl} + \tilde{w}_{jl} + \tilde{N}_{T,jl} = \frac{1}{RePr} \tilde{\nabla}_{jl}^2 \tilde{T}_{jl}, \quad (2.22)$$

where $\tilde{N}_{r,jl}$, $\tilde{N}_{\theta,jl}$, $\tilde{N}_{z,jl}$ and $\tilde{N}_{T,jl}$ are the terms convoluted from the nonlinear terms (2.11)–(2.14) using the Fourier transform and $\tilde{\nabla}_{jl}^2 = \partial^2/\partial r^2 + (1/r)\partial/\partial r - k_l^2 - m_j^2/r^2$ is the modal Laplacian operator. For the boundary conditions, we consider

$$\tilde{u}_{jl} = \tilde{v}_{jl} = \tilde{w}_{jl} = \frac{\partial \tilde{T}_{jl}}{\partial r} = 0, \quad (2.23)$$

at both cylinders $r = 1$ and $r = 1/\eta$.

An advantage of using the equations in a modal form is that (2.18)–(2.22) can further be simplified by eliminating the pressure \tilde{p}_{jl} as follows:

$$\mathcal{A}_{jl} \frac{\partial \tilde{\mathbf{q}}_{jl}}{\partial t} = \mathcal{B}_{jl} \tilde{\mathbf{q}}_{jl} + \tilde{\mathbf{N}}_{jl}, \quad (2.24)$$

where $\tilde{\mathbf{q}}_{jl}$ is the vector of three variables, \mathcal{A}_{jl} and \mathcal{B}_{jl} are the differential operator matrices and $\tilde{\mathbf{N}}_{jl}$ is the vector comprised of the nonlinear terms, all of which depend on indices j and l such as whether $l = 0$ or not and whether $j = 0$ or not. We refer the reader to [Appendix A](#) for more details of these vectors and matrices. For spatial discretisation in the radial direction r , a spectral method using the Chebyshev collocation points is considered (Antkowiak & Brancher 2004; Park 2012). The vector $\tilde{\mathbf{N}}_{jl}$ is computed at each step using a pseudo-spectral method, similar to that in Deloncle *et al.* (2008). Equation (2.24) is written in a spectral form in the azimuthal and axial directions and we use the backward Fourier transform to obtain the vector \mathbf{q}_{jl} in the physical space (r, θ, z) . Then \mathbf{q}_{jl} is used to compute the nonlinear term \mathbf{N}_{jl} in the physical space and apply the forward Fourier transform to \mathbf{N}_{jl} to compute $\tilde{\mathbf{N}}_{jl}$ in the spectral space (r, m_j, k_l) . In this pseudo-spectral approach, we consider the numbers of collocation points $N_\theta = 2M + 1$ and $N_z = 2K + 1$ in the azimuthal and axial directions, respectively. The pseudo-spectral approach is similar to that in Guseva *et al.* (2015) who also consider the axial periodicity with the Fourier method but utilise a fractional time-stepping method by carefully computing an intermediate pressure using the influence-matrix method, which is especially effective in solving equations for the magnetic field. On the contrary, we avoid the use of the pressure \tilde{p}_{jl} by considering different operator matrices \mathcal{A}_{jl} and \mathcal{B}_{jl} that depend on the indices j and l . Unlike Deloncle *et al.* (2008), the de-aliasing technique, which is required in turbulence simulations, is not implemented as the Reynolds number Re_i considered in this work is not large enough to observe small-scale turbulence. For time advancement, we use a conventional semi-implicit scheme (see e.g. Kim *et al.* 1987) with the Crank–Nicolson method for the linear term and the Adam–Bashforth method for the nonlinear term. For instance, at each step n , we find the next step solution $\tilde{\mathbf{q}}_{jl}^{(n+1)}$ by solving numerically the discretised version of (2.24):

$$\left(\mathcal{A}_{jl} - \frac{\Delta t}{2} \mathcal{B}_{jl} \right) \tilde{\mathbf{q}}_{jl}^{(n+1)} = \left(\mathcal{A}_{jl} + \frac{\Delta t}{2} \mathcal{B}_{jl} \right) \tilde{\mathbf{q}}_{jl}^{(n)} + \frac{\Delta t}{2} \left(3\tilde{\mathbf{N}}_{jl}^{(n)} - \tilde{\mathbf{N}}_{jl}^{(n-1)} \right), \quad (2.25)$$

where Δt is the time step. In this study, the time step Δt is fixed to $\Delta t = 0.01$, which is found to be sufficiently small for parameters considered in this study. It is verified that the Courant–Friedrichs–Lewy condition for perturbation velocity is satisfied and every DNS demonstrates no numerical divergence with this Δt .

2.3. One-dimensional local linear stability analysis

By assuming that the perturbation is infinitesimally small, we can neglect nonlinear terms and perform 1-D local LSA using the normal mode:

$$\begin{pmatrix} u_r \\ u_\theta \\ u_z \\ T \\ p \end{pmatrix} = \begin{pmatrix} \hat{u}(r) \\ \hat{v}(r) \\ \hat{w}(r) \\ \hat{T}(r) \\ \hat{p}(r) \end{pmatrix} \exp(im\theta + ikz - i\omega t) + \text{c.c.}, \quad (2.26)$$

where c.c. denotes the complex conjugate, \hat{u} , \hat{v} , \hat{w} , \hat{p} and \hat{T} are the mode shapes, m is the azimuthal wavenumber, k is the axial wavenumber and ω is the complex frequency $\omega = \omega_r + i\omega_i$, where $\omega_r = \text{Re}(\omega)$ is the temporal frequency and $\omega_i = \text{Im}(\omega)$ is the temporal growth rate. Throughout the paper, the non-dimensional wavenumber $k_d = kd/R_i = k(1 - \eta)/\eta$ rescaled by the gap size d is also used for convenience in comparison with other literature. The normal mode (2.26) is applied to (2.6)–(2.10) with the nonlinear terms neglected and, after manipulations, we can eliminate the pressure mode shape and obtain the following simplified eigenvalue problem:

$$-i\omega \mathcal{A} \hat{\mathbf{q}} = \mathcal{B} \hat{\mathbf{q}}, \quad (2.27)$$

where $\hat{\mathbf{q}} = (\hat{u}, \hat{v}, \hat{T})^T$ and \mathcal{A} and \mathcal{B} are the operator matrices, which are essentially the same as \mathcal{A}_{11} and \mathcal{B}_{11} , respectively, the operator matrices in (2.24) with $j = l = 1$. To solve the eigenvalue problem (2.27), the MATLAB routine eig is used with the following boundary conditions imposed at both cylinders $r = 1$ and $r = 1/\eta$:

$$\hat{u} = \hat{v} = \hat{w} = \frac{d\hat{T}}{dr} = 0. \quad (2.28)$$

The Chebyshev spectral method is used for discretisation in the radial direction r and a number of collocation points N_r between 60 and 120 is considered in this study. The choice of N_r depends on how large are the parameters such as the Reynolds number Re or the Péclet number $Pe = RePr$, how the eigenmodes are confined near the boundaries, etc. For more details of the LSA and numerical methods, we refer the reader to our previous work (e.g. Park 2012; Park & Billant 2013) that used the same code.

2.4. Two-dimensional bi-global linear stability analysis

For parameters considered in this study, 1-D LSA reveals that the axisymmetric mode with $m = 0$ is the most unstable one for cylindrical Couette flow. As demonstrated in the next sections, centrifugal instability develops nonlinearly and saturates leading to axisymmetric Taylor vortices as a new base state. The new 2-D base state $\bar{\mathbf{Q}}(r, z) = (\bar{\mathbf{U}}, \bar{T})$ is comprised of the new base velocity $\bar{\mathbf{U}}(r, z) = (\bar{U}(r, z), \bar{V}(r, z), \bar{W}(r, z))$ and the new base temperature $\bar{T}(r, z)$. For this Taylor vortex flow, we can analyse its secondary instability through 2-D bi-global LSA by considering a non-axisymmetric perturbation $\bar{\mathbf{q}}$ with $m \neq 0$ expressed in the following ansatz:

$$\bar{\mathbf{q}} = \begin{pmatrix} \bar{u}_r \\ \bar{u}_\theta \\ \bar{u}_z \\ \bar{T} \\ \bar{p} \end{pmatrix} = \begin{pmatrix} \hat{u}_m(r, z) \\ \hat{v}_m(r, z) \\ \hat{w}_m(r, z) \\ \hat{T}_m(r, z) \\ \hat{p}_m(r, z) \end{pmatrix} \exp(im\theta - i\omega_m t) + \text{c.c.}, \quad (2.29)$$

where \hat{u}_m , \hat{v}_m , \hat{w}_m , \hat{T}_m and \hat{p}_m are the 2-D global mode shapes and ω_m is the complex frequency of the global mode. Similar to the 1-D local LSA, an eigenvalue problem can be formulated as

$$-i\omega_m \mathcal{A}_m \hat{\mathbf{q}}_m = \mathcal{B}_m \hat{\mathbf{q}}_m, \quad (2.30)$$

where \mathcal{A}_m and \mathcal{B}_m are the operator matrices detailed in [Appendix A.2](#) and $\hat{\mathbf{q}}_m = (\hat{u}_m, \hat{v}_m, \hat{T}_m)^T$ is the mode shape. The matrices \mathcal{A}_m and \mathcal{B}_m in the 2-D bi-global LSA have a much larger size than the size of the matrices \mathcal{A} and \mathcal{B} in (2.27). Thus we use the MATLAB routine `eigs` that computes only a few eigenvalues near a specified value using the Krylov–Schur algorithm (Stewart 2002). To solve the eigenvalue problem (2.30), we consider the following boundary conditions:

$$\hat{u}_m = \hat{v}_m = \hat{w}_m = \frac{\partial \hat{T}_m}{\partial r} = 0. \quad (2.31)$$

The Chebyshev and Fourier spectral methods are used for discretisation in the radial and axial directions, respectively. The Fourier method imposes the periodic boundary condition in the axial direction z given that the axisymmetric Taylor vortices as a new base state are also periodic in z with wavelength $\lambda_z = 2\pi/k$.

3. Linear centrifugal instability in stratified and diffusive fluids

Linear instability of stratified flows in thermally diffusive fluids, especially with low Pr , has been investigated for various planar shear flows in a linear profile (Barker *et al.* 2019, 2020; Dymott *et al.* 2023), a periodic sinusoidal profile (Chang & Garaud 2021; Garaud *et al.* 2024b) and a hyperbolic tangent profile (Park *et al.* 2020, 2021b). They consider flows with vertical shear, horizontal shear or mixed shear (where the ‘vertical’ direction in these studies implies the direction of gravity and stratification) and investigate linear and nonlinear properties of shear instabilities. In this section, we similarly investigate linear centrifugal instability of Taylor–Couette flow, a horizontally sheared rotating flow, in stratified and diffusive fluids. The linear analysis results are followed by nonlinear simulation results presented in §4.

3.1. Neutral stability curves

[Figure 2\(a\)](#) shows the growth rate ω_i of the axisymmetric mode ($m = 0$), which is found to be most unstable, versus the wavenumber k_d for different parameter sets of (N, Pr) at $\mu = 0$, $\eta = 0.9$ and $Re_i = 200$. For every case presented in [figure 2\(a\)](#), the corresponding frequency ω_r is zero. It is known that centrifugal instability reaches its maximum $\omega_{i,max}$ as $k \rightarrow \infty$ in the inviscid limit $Re \rightarrow \infty$ as the growth rate scales as $\omega_{i,inviscid} = \omega_{i,max} - A_0/k^2$ (Billant & Gallaire 2005; Park *et al.* 2017) while the viscous growth rate scales as $\omega_{i,viscous} = \omega_{i,inviscid} - A_1 k^2/Re$ (Yim *et al.* 2016), where A_0 and A_1 are positive constants that depend on stratification and other parameters. Due to this characteristic varying with k , the viscous growth rates are positive in a finite range of k_d and each curve reaches its peak at a certain wavenumber $k_{d,max}$. As the stratification increases from $N = 0$ (grey) to $N = 1$ (black) for $Pr = 1$, the growth-rate curves descend while the wavenumber $k_{d,max}$ at the peak of ω_i increases. For fixed $N = 1$, as the Prandtl number Pr decreases from $Pr = 1$, the growth rate increases and, remarkably, the growth-rate curves for $Pr = 10^{-2}$ and 10^{-4} overlap with the grey curve, the unstratified case with $N = 0$. This implies that the centrifugal instability in stratified and highly diffusive fluids with $Pr \ll 1$ behaves as the instability in unstratified fluids as the effect of stratification is suppressed

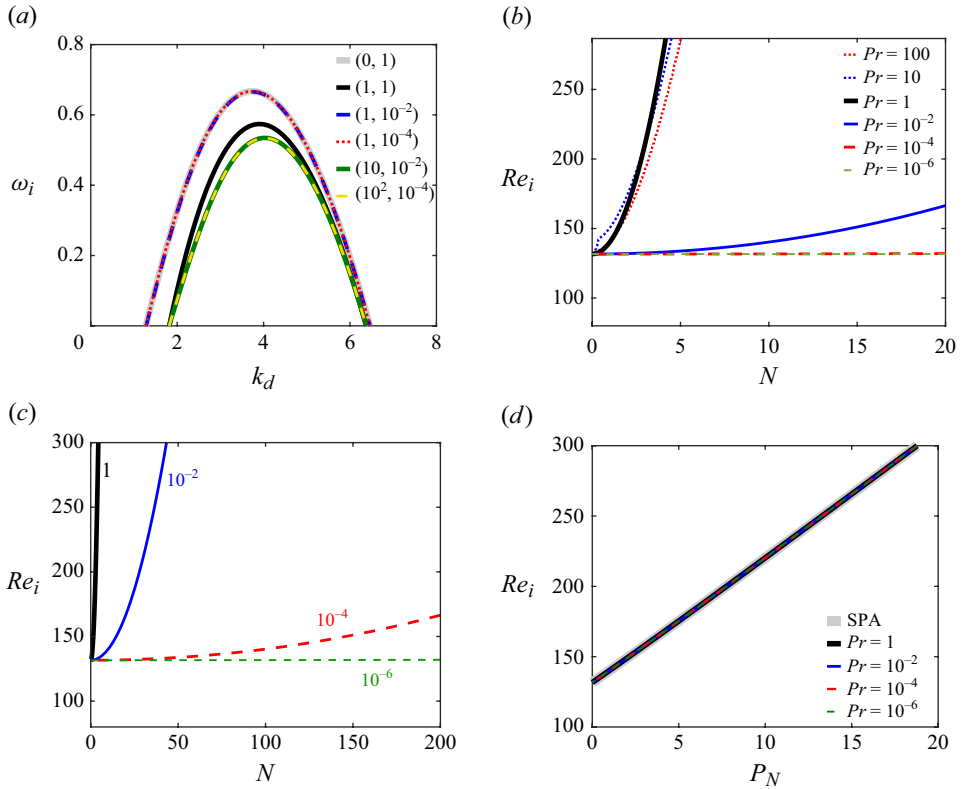


Figure 2. (a) Growth-rate curves for various sets of (N, Pr) at $\mu = 0$, $\eta = 0.9$, $Re_i = 200$ and $m = 0$. (b) Neutral stability curves in the parameter space (N, Re_i) for different Pr at $\mu = 0$, $\eta = 0.9$ and $m = 0$. (c) The curves for different Pr same as (b) but over a wider range of N . (d) The curves same as (c) overlapped due to the rescaled parameter $P_N = N^2 Pr$ on the abscissa. An additional thick grey line is a neutral stability curve obtained from the small- Pr approximation.

by strong thermal diffusion. Another remarkable result in figure 2(a) is that the growth-rate curves overlap for $(N, Pr) = (10, 10^{-2})$ and $(10^2, 10^{-4})$, the cases with the same $P_N = N^2 Pr = 1$. The growth rate for other values of N and $Pr \ll 1$ is invariant if the rescaled parameter P_N is the same. Such an invariant feature at the same P_N but different N and Pr is similarly reported for both vertical and horizontal shear instabilities in vertically stratified fluids (Lignières *et al.* 1999; Park *et al.* 2020, 2021b).

Figure 2(b) display neutral stability curves, which denote the critical Reynolds number $Re_{i,c}$ at which the growth rate ω_i of the most unstable mode is zero, in the parameter space (N, Re_i) for different values of Pr at $\mu = 0$, $\eta = 0.9$ and $m = 0$. For $Pr \geq 1$, the neutral stability curves increase rapidly with N , a feature similarly found in Park *et al.* (2017), and the $Pr = 1$ case is more stable than other cases with $Pr > 1$ when $N > 3$. This is expected as thermal dissipation is proportional to the diffusivity κ_0 ; thus lower diffusivity κ_0 (i.e. higher Pr) implies less thermal dissipation and more instability. In the range $0 < N < 3$, the situation is more complicated since the $Pr = 10$ case is more stable than other Pr cases for the axisymmetric perturbation. Although such high- Pr dynamics at a moderate N should be further investigated due to its great importance in geophysical and other contexts (e.g. oceanic flows where the analogous Schmidt number Sc is around 700), the current study will only focus on the highly diffusive regime with low $Pr \leq 1$. For $Pr < 1$, the curves increase very slowly as N increases and it is difficult to see in figure 2(b) the

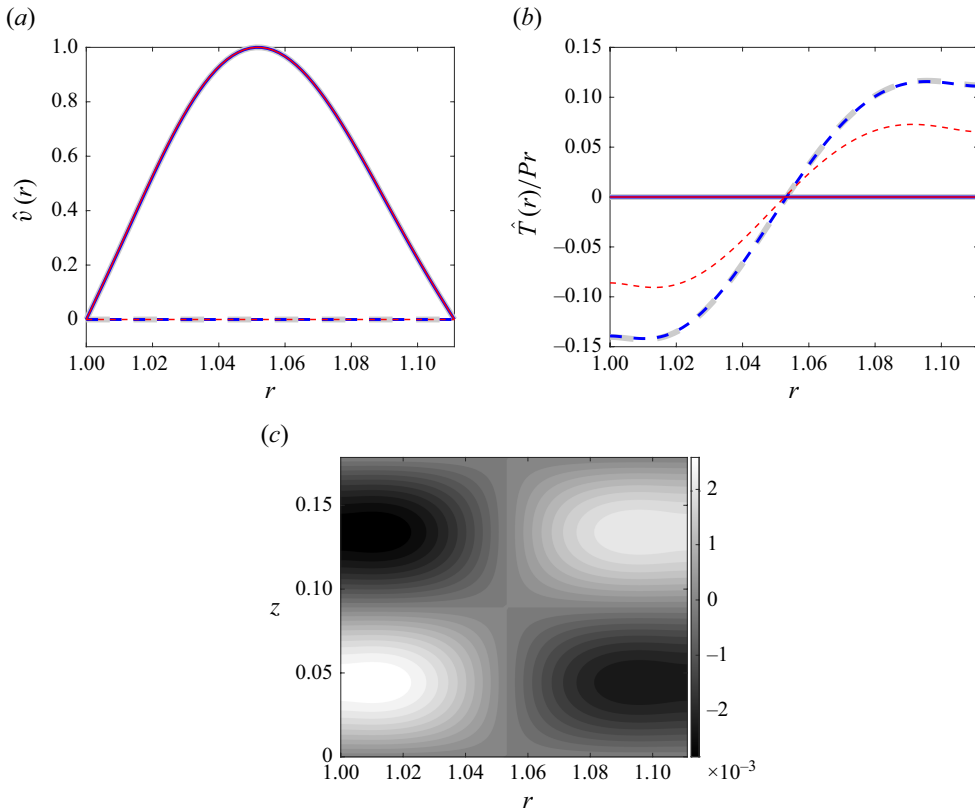


Figure 3. (a,b) Real (solid) and imaginary (dashed) parts of the mode shape $\hat{v}(r)$ and rescaled mode $\hat{T}(r)/Pr$ for $Pr = 1$ (red), $Pr = 10^{-2}$ (blue) and $Pr = 10^{-4}$ (grey) at $\mu = 0$, $\eta = 0.9$, $Re_i = 200$, $N = 1$, $m = 0$ and $k_d = 3.91$. (c) Perturbation temperature $T(r, z)$ reconstructed from $\hat{T}(r)$ for $Pr = 10^{-2}$.

increase of the curves at $Pr = 10^{-4}$ and 10^{-6} over the range $0 \leq N \leq 20$. Figure 2(c) displays the same neutral stability curves for $Pr \leq 1$ over a wider range of N to see how slowly the neutral stability curves increase with N as Pr decreases. This increasing trend confirms that, while stratification enhances the stability of stratified Taylor–Couette flow, strong thermal diffusion destabilises by preventing the stabilising role of stratification and making the flow behave like an unstratified flow. In figure 2(d), we plot again the same neutral stability curves but over the rescaled parameter P_N on the abscissa. All the curves now overlap each other, even for the case with $Pr = 1$, and can be described by a linear relation as $Re_{i,c} = 131.6 + 8.965 P_N$, where $Re_{i,c} = 131.6$ is the critical Reynolds number for the unstratified case $N = 0$ at $m = 0$ and $\eta = 0.9$, the number agreeing with DiPrima *et al.* (1984).

Figure 3 shows the real and imaginary parts of eigenmode shapes $\hat{v}(r)$ and $\hat{T}(r)$ for different Pr for the wavenumber set $(m, k_d) = (0, 3.91)$. The mode shapes are normalised by the maximum value of \hat{v} and it is found that the mode shape \hat{T} has a smaller amplitude than \hat{v} for small Pr . As the Prandtl number Pr decreases, the amplitude of \hat{T} decreases and scales as $O(Pr)$. For a better comparison, figure 3(b) displays the mode shape $\hat{T}(r)$ divided by Pr and we see that the rescaled \hat{T}/Pr has the same mode shape for the cases with $Pr = 10^{-2}$ and $Pr = 10^{-4}$. In figure 3(c), the perturbation temperature $T(r, z) = \hat{T} \exp(ikz) + \hat{T}^* \exp(-ikz)$ for $Pr = 10^{-2}$ is plotted. Two in-phase waves,

one near the inner cylinder and the other near the outer one, are clearly shown. The shape of this axisymmetric mode is different from that of a non-axisymmetric centrifugal instability mode, which is weakly sheared, or that of a SRI mode that is out of phase (Park *et al.* 2017, 2018). The perturbation temperature has one node (i.e. the zero crossing) around $r \simeq 1.053$ as it is the first mode which becomes the most unstable. Higher-order modes with a greater number of nodes are, on the other hand, found to be stable for the parameter set in figure 3 with $Pr = 10^{-2}$.

3.2. Small- Pr approximation

The single dependence on P_N for different N and Pr in the limit $Pr \ll 1$ can be understood by taking the small- Pr approximation. Consider the Taylor expansions in terms of small Pr as $\hat{\mathbf{u}} = (\hat{u}, \hat{v}, \hat{w})^T = \hat{\mathbf{u}}^{(0)} + Pr\hat{\mathbf{u}}^{(1)} + O(Pr^2)$ and similarly for \hat{T} and \hat{p} as $\hat{T} = \hat{T}^{(0)} + Pr\hat{T}^{(1)} + \dots$ and $\hat{p} = \hat{p}^{(0)} + Pr\hat{p}^{(1)} + \dots$. For the Péclet number Pe being small, $Pe = RePr \ll 1$ (i.e. $Re \sim O(1)$ and $Pr \ll 1$), we obtain the leading-order equation for $\hat{T}^{(0)}$ as

$$\frac{1}{RePr} \hat{\nabla}^2 \hat{T}^{(0)} = 0, \quad (3.1)$$

which leads to the analytic solution $\hat{T}^{(0)}(r) = a_1 I_m(kr) + a_2 K_m(kr)$, where a_1 and a_2 are constants and I_m and K_m are modified Bessel functions of the first and second kinds, respectively (Abramowitz & Stegun 1965). The constants a_1 and a_2 become zero if the no-flux conditions $d\hat{T}^{(0)}/dr = 0$ are imposed at both cylinders; thus the leading-order solution simply becomes zero (i.e. $\hat{T}^{(0)}(r) = 0$). At the next order, we obtain the following equations:

$$\frac{d\hat{u}^{(0)}}{dr} + \frac{\hat{u}^{(0)}}{r} + \frac{im\hat{v}^{(0)}}{r} + ik\hat{w}^{(0)} = 0, \quad (3.2)$$

$$-i\omega\hat{u}^{(0)} + im\Omega\hat{u}^{(0)} - 2\Omega\hat{v}^{(0)} = -\frac{d\hat{p}^{(0)}}{dr} + \frac{1}{Re} \left(\hat{\nabla}^2 \hat{u}^{(0)} - \frac{\hat{u}^{(0)}}{r^2} - \frac{2im\hat{v}^{(0)}}{r^2} \right), \quad (3.3)$$

$$-i\omega\hat{v}^{(0)} + im\Omega\hat{v}^{(0)} + Z\hat{u}^{(0)} = -\frac{im\hat{p}^{(0)}}{r} + \frac{1}{Re} \left(\hat{\nabla}^2 \hat{v}^{(0)} - \frac{\hat{v}^{(0)}}{r^2} + \frac{2im\hat{u}^{(0)}}{r^2} \right), \quad (3.4)$$

$$-i\omega\hat{w}^{(0)} + im\Omega\hat{w}^{(0)} = -ik\hat{p}^{(0)} + P_N\hat{T}^{(1)} + \frac{1}{Re} \hat{\nabla}^2 \hat{w}^{(0)}, \quad (3.5)$$

$$\hat{w}^{(0)} = \frac{1}{Re} \hat{\nabla}^2 \hat{T}^{(1)}, \quad (3.6)$$

where $P_N = N^2 Pr$. We see that the two parameters N and Pr representing thermal stratification and diffusion are simplified into a single parameter P_N , as observed in other studies under the small-Péclet-number approximation (e.g. Lignières 1999; Park *et al.* 2020). By considering the continuity equation and eliminating the pressure, (3.2)–(3.6) can further be simplified into the following eigenvalue problem:

$$-i\omega\mathcal{A}^{(0)}\hat{\mathbf{q}}^{(0)} = \mathcal{B}^{(0)}\hat{\mathbf{q}}^{(0)}, \quad (3.7)$$

where $\hat{\mathbf{q}}^{(0)}$ is the mode shape vector and $\mathcal{A}^{(0)}$ and $\mathcal{B}^{(0)}$ are the operator matrices detailed in Appendix A. In figure 2(d), it is clearly shown that a neutral stability curve computed from (3.7) overlaps with other neutral stability curves when they are plotted over the rescaled Prandtl number $P_N = N^2 Pr$ as the abscissa.

3.3. Perturbation energy analysis

The instability characteristics can also be understood by examining the evolution of perturbation energy. We first define the total perturbation energy $E(t)$ as

$$E(t) = \frac{1}{2} \int_0^{L_z} \int_0^{2\pi} \int_1^{1/\eta} \left(u_r^2 + u_\theta^2 + u_z^2 + N^2 T^2 \right) r \, dr \, d\theta \, dz = \frac{1}{2} \langle \mathbf{q}_E : \mathbf{q}_E \rangle, \quad (3.8)$$

where L_z is a vertical length of the domain assumed to be periodic (e.g. $L_z = 2\pi/k$ if we consider one periodic length of a normal mode with the axial wavenumber k), the angle brackets denote the volume integral defined as $\langle \mathbf{X} \rangle = \int_0^{L_z} \int_0^{2\pi} \int_1^{1/\eta} \mathbf{X} r \, dr \, d\theta \, dz$, $\mathbf{q}_E = (u_r, u_\theta, u_z, NT)^T$ and $:$ denotes the Frobenius product (for more details, see also Park *et al.* 2017). For the momentum and energy equations (2.7)–(2.10), we multiply both sides by $(u_r, u_\theta, u_z, N^2 T)^T$ and, after some manipulations, we obtain the following equation for perturbation energy:

$$\frac{\partial E}{\partial t} = \left\langle -\frac{d\Omega}{dr} (ru_r u_\theta) - \frac{1}{Re} \left[\nabla \mathbf{u} : \nabla \mathbf{u} + \frac{N^2}{Pr} (\nabla T : \nabla T) \right] \right\rangle, \quad (3.9)$$

where the first term on the right-hand side within the angle brackets denotes the contribution from the mean angular shear $d\Omega/dr$ and the second term corresponds to the kinetic and potential energy dissipation. The contribution from the mean angular shear is a main source of energy production if the momentum transfer term $u_r u_\theta$ is anti-correlated with the mean angular shear $d\Omega/dr$, a well-known mechanism for instability called the Orr mechanism (Orr 1907). The momentum and thermal dissipation terms are always negative and thus stabilise the perturbation energy. We note that this mechanism is valid for both linear and nonlinear cases as the evolution equation (3.9) is derived from the nonlinear perturbation equations (2.7)–(2.10) and the nonlinear terms are cancelled out in the derivation process in which continuity is taken into account. If we apply the normal mode (2.26) to the evolution equation (3.9), we obtain the following expression for the growth rate:

$$\omega_i = \frac{1}{\hat{E}} \left\langle -\frac{d\Omega}{dr} r \frac{(\hat{u}^* \hat{v} + \hat{u} \hat{v}^*)}{2} - \frac{1}{Re} \left[\hat{\nabla} \hat{\mathbf{u}} : \hat{\nabla} \hat{\mathbf{u}} + \frac{N^2}{Pr} (\hat{\nabla} \hat{T} : \hat{\nabla} \hat{T}) \right] \right\rangle_r, \quad (3.10)$$

where $*$ denotes the complex conjugate, $\langle \rangle_r$ denotes the line integral over the radial coordinate r as $\langle \hat{\mathbf{X}} \rangle_r = \int_1^{1/\eta} \hat{\mathbf{X}} r \, dr$ and $\hat{E} = \langle |\hat{u}|^2 + |\hat{v}|^2 + |\hat{w}|^2 + |N\hat{T}|^2 \rangle_r$.

Table 1 presents examples of the maximum growth rate $\omega_{i,max}$ and corresponding wavenumber $k_{d,max}$ for various parameter sets of (N, Pr, m) at $\mu = 0$, $\eta = 0.9$ and $Re_i = 200$. The table also details the production and dissipation terms \mathcal{P}_Ω , ϵ_k and ϵ_p , which are defined as

$$\mathcal{P}_\Omega = \left\langle -\frac{d\Omega}{dr} r \frac{(\hat{u}^* \hat{v} + \hat{u} \hat{v}^*)}{2} \right\rangle_r, \quad \epsilon_k = -\frac{1}{Re} \langle \hat{\nabla} \hat{\mathbf{u}} : \hat{\nabla} \hat{\mathbf{u}} \rangle_r, \quad \epsilon_p = -\frac{N^2}{Re Pr} \langle \hat{\nabla} \hat{T} : \hat{\nabla} \hat{T} \rangle_r. \quad (3.11)$$

N	Pr	m	$k_{d,max}$	$\omega_{i,max}$	$\mathcal{P}_\Omega/\hat{E}$	ϵ_k/\hat{E}	ϵ_p/\hat{E}	$(\mathcal{P}_\Omega + \epsilon_k + \epsilon_p)/\hat{E}$
0	1	0	3.74	0.667	1.813	-1.146	0	0.667
1	1	0	3.91	0.574	1.769	-1.185	-0.010	0.574
1	1	1	3.90	0.564	1.763	-1.188	-0.011	0.564
1	10^{-2}	0	3.74	0.666	1.808	-1.142	-0.0003	0.666
10	10^{-2}	0	4.03	0.535	1.791	-1.236	-0.020	0.535

Table 1. Values of the maximum growth rates $\omega_{i,max}$ with the corresponding wavenumber $k_{d,max}$, production and dissipation terms for various N , Pr and m at $\mu = 0$, $\eta = 0.9$ and $Re_i = 200$.

The production and dissipation terms are calculated by implementing the eigenfunction into the expressions (3.11) and their sum shows a good agreement with the eigenvalue $\omega_{i,max}$. For every case, the contribution from the thermal dissipation ϵ_p to the growth rate is small as $Pr \leq 1$ and the growth rate ω_i is mainly determined by a difference between the production \mathcal{P}_Ω and the viscous dissipation ϵ_k . For the cases with $Pr \ll 1$, if we apply the small- Pr approximation, we can re-express the thermal dissipation ϵ_p as

$$\epsilon_p \simeq -\frac{P_N}{Re} \left\langle \hat{\nabla} \hat{T}_1 : \hat{\nabla} \hat{T}_1 \right\rangle_r \sim O\left(\frac{P_N}{Re}\right), \quad (3.12)$$

where the dependence on the two parameters N and Pr is now expressed by the single parameter P_N under the small- Pr approximation. The scaling for thermal dissipation $\epsilon_p \sim O(P_N/Re)$ is based on the assumption $\hat{T}_1 \sim O(1)$ under the small- Pr approximation.

3.4. Parametric investigations

Figures 4(a) and 4(b) show neutral stability curves for axisymmetric and non-axisymmetric cases in the parameter space (N , Re_i) at $\mu = 0$ and $\eta = 0.9$ for $Pr = 1$ and 10^{-4} , respectively. For both Pr values, all the neutral stability curves increasing with N ascend as m increases; thus the lowest curves correspond to the axisymmetric case with $m = 0$. A difference between the two Pr values is that, for $Pr = 1$, neutral stability curves for non-axisymmetric cases ($m > 0$) stay closer to the curve for the axisymmetric case ($m = 0$) as N increases, while for $Pr = 10^{-4}$, the curves for $m > 0$ stay further from the curve for $m = 0$ as N increases. This implies that for strongly stratified fluids with $N \gg 0$ for $Pr = 1$, the axisymmetric mode will appear at the instability onset $Re_i = Re_{i,c}$ but then non-axisymmetric perturbations will also become unstable immediately after the onset; thus competition between the axisymmetric and non-axisymmetric modes will occur right above $Re_i > Re_{i,c}$. On the other hand, for low Pr and above the instability onset $Re_i > Re_{i,c}$, the axisymmetric mode will become more dominant over non-axisymmetric modes as N increases. Figure 4(c) displays neutral stability curves over the rescaled P_N for different Pr at $m = 2$. As similarly observed for the axisymmetric case $m = 0$ in figure 2(c), the curves for $Pr \leq 10^{-2}$ overlap and agree with the prediction from the small- Pr approximation. It is found that the line from the small- Pr approximation for $m = 2$ scales as $Re_{i,c} = 134.4 + 9.971 P_N$, where $Re_c = 134.4$ as the Re_i -axis intercept at $P_N = 0$ corresponds to the critical Reynolds number for unstratified case $N = 0$. The slope 9.971 for $m = 2$ is higher than the slope 8.965 of the $m = 0$ case. It is verified that the critical Reynolds number and the slope increase with m and thus they are at the lowest for $m = 0$. This implies that for low Pr , the axisymmetric mode with $m = 0$ is expected to be the most unstable one for $P_N = N^2 Pr \geq 0$.

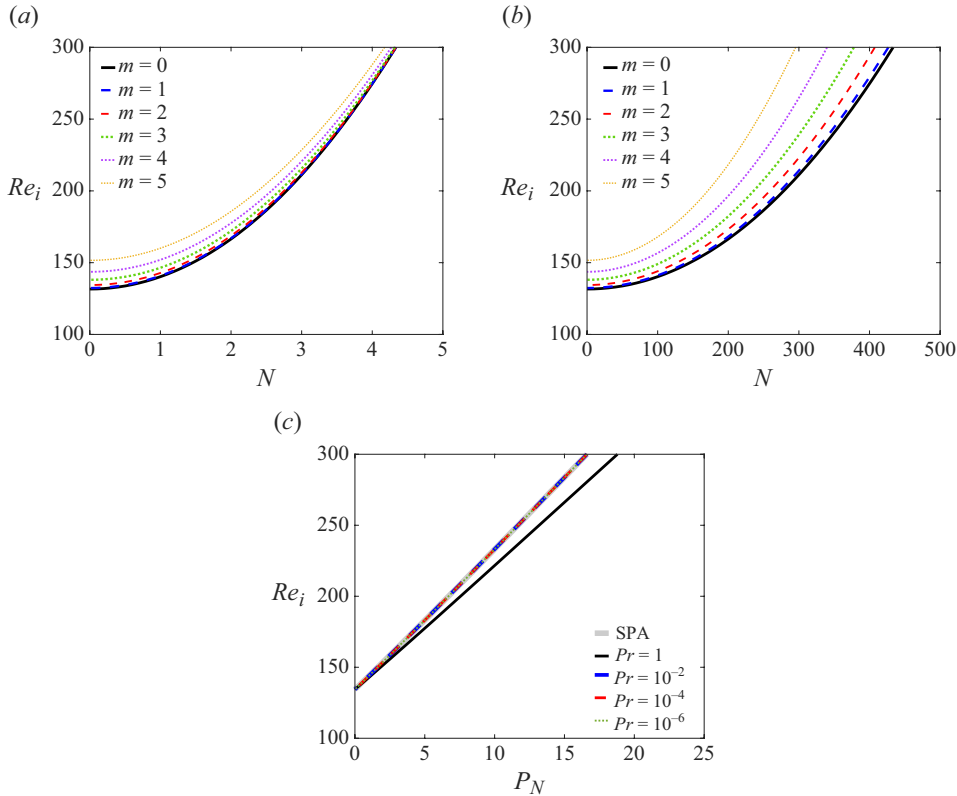


Figure 4. Neutral stability curves for different m for (a) $Pr = 1$ and (b) $Pr = 10^{-4}$ at $\mu = 0$ and $\eta = 0.9$. (c) Neutral stability curves for different Pr over the rescaled parameter P_N at $\mu = 0$, $\eta = 0.9$ and $m = 2$. A thick grey line denotes the neutral stability curve from the small- Pr approximation (SPA).

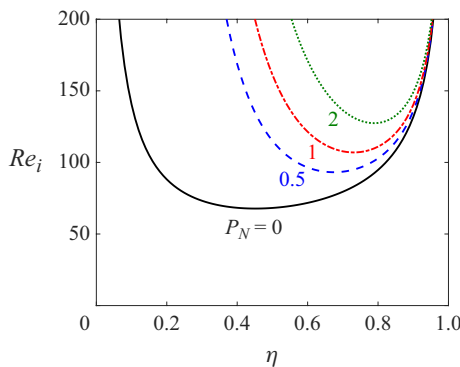


Figure 5. Neutral stability curves obtained from the small- Pr approximation at $\mu = 0$.

Figure 5 shows neutral stability curves obtained from the small- Pr approximation in the wide parameter space (η, Re_i) for different values of P_N at $\mu = 0$. The curve for $P_N = 0$ agrees with the result in DiPrima *et al.* (1984). The azimuthal wavenumber of the curves corresponds to $m = 0$ as the axisymmetric perturbation is found to be more unstable than non-axisymmetric perturbations. An advantage of using the small- Pr approximation is

Case	Re_i	N	Pr	N_r	N_θ	N_z	k	k_d	L_z	\mathcal{R}_c
1	145	1	1	60	33	33	30.6	3.40	$2\pi/k$	1.035
2	200	1	0.01	120	65	65	28.2	3.13	$2\pi/k$	1.519
3	200	1	1	120	65	65	30.6	3.40	$2\pi/k$	1.427

Table 2. Physical and numerical parameters for representative 3-D DNS cases.

that, for $Pr \ll 1$, the stability curves depend solely on a single parameter $P_N = N^2 Pr$ instead of two parameters N and Pr ; thus parametric investigations become simplified. As P_N increases, the curves ascend and, in particular, the wide-gap Taylor–Couette flow with small η is strongly stabilised. It is also shown that the curves are less sensitive to the change in P_N when η is close to 1 (i.e. Taylor–Couette flow with a small gap).

This section has described how linear centrifugal instability of stratified Taylor–Couette flow is affected by strong thermal diffusion. It is shown that the stratification having a stabilising effect on the instability is suppressed by strong thermal diffusion. For the cases with $Pr \ll 1$, the dependence on N and Pr is simplified further by a single rescaled parameter $P_N = N^2 Pr$ as derived by the small- Pr approximation. In § 4, we study how the instability modes develop nonlinearly in stratified and diffusive fluids. Nonlinear dynamical behaviours such as nonlinear saturation, secondary instability of the saturated state or transition to chaotic states are examined.

4. Nonlinear development of centrifugal instability

In this section, we investigate via DNS how the centrifugal instability develops nonlinearly. Table 2 provides details of physical and numerical parameters used for the main 3-D DNS cases that are thoroughly analysed. There are more 3-D and 2-D DNS results with similar parameters in the paper; however, we focus on the analysis of these three main cases featuring nonlinear saturation, secondary instability and transition to chaotic states. These nonlinear features are thoroughly discussed in the following subsections. In the table, parameters to be noted are the axial wavenumber k and the domain length $L_z = 2\pi/k$ (i.e. one periodic length). The wavenumber k in table 2 is chosen as $k = k_c$, which is the critical wavenumber at the critical Reynolds number $Re_i = Re_{i,c}$ at the onset of primary instability. This wavenumber choice is coherent with previous studies that investigated axisymmetric Taylor vortices for $Re_i > Re_{i,c}$ by considering the characteristic wavenumber k close to k_c as $k \simeq k_c$, although a better agreement with experiments can be met for the torque of Taylor-vortex flow and wavy-vortex flow at high $Re_i \gg Re_{i,c}$ if a suitable variation of the wavenumber is taken into account (see e.g. Meyer 1966; Davey *et al.* 1968; DiPrima *et al.* 1984). Our study considers the Reynolds number Re_i not too far from $Re_{i,c}$ (i.e. the Reynolds-number ratio $\mathcal{R}_c = Re_i/Re_{i,c} < 2$); thus the flow is not turbulent. In this case, the choices of the wavenumber $k = k_c$ and the corresponding domain length $L_z = 2\pi/k$ are seemingly appropriate for comparison with other studies. We support this presumption by providing in Appendix B the validation against experiments and numerical verification of the domain length dependence. The principal azimuthal wavenumber m in DNS is $m = 1$ so that the entire angle $\theta = [0, 2\pi]$ with its azimuthal periodicity is considered as the azimuthal domain.

If the Fourier representation (2.17) is taken into account, the perturbation energy $E(t)$ can be expressed as the sum: $E(t) = \sum_{j=-M}^M \sum_{l=-K}^K \tilde{E}_{jl}(t)$, where \tilde{E}_{jl} is the modal

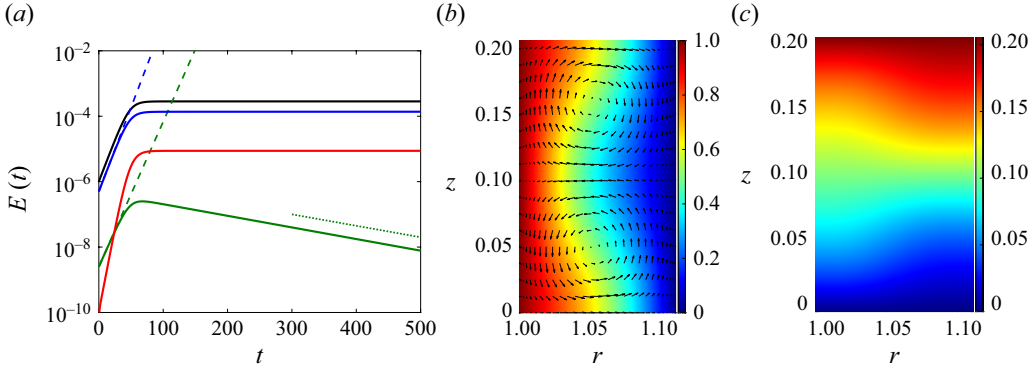


Figure 6. (a) Time evolution of the total energy $E(t)$ (black) and representative modal energy components: \tilde{E}_{01} (blue), \tilde{E}_{11} (green) and \tilde{E}_{00} (red) for case 1. The dashed lines denote 1-D LSA predictions on the growth of the modes with $(m = 0)$ (blue) and $m = 1$ (green). The green dotted line denotes a 2-D bi-global LSA prediction on the decay of the non-axisymmetric mode $(m = 1)$. (b) Velocity field on the plane (r, z) at $\theta = 0$ and $t = 500$ with contours denoting the total azimuthal velocity U_θ and vector plot denoting the transverse velocity field (u_r, u_z) . (c) The total temperature profile $\Theta(r, z)$ at $t = 500$.

energy defined as

$$\tilde{E}_{jl} = \pi L_z \int_1^{1/\eta} \left(|\tilde{u}_{jl}|^2 + |\tilde{v}_{jl}|^2 + |\tilde{w}_{jl}|^2 + N^2 |\tilde{T}_{jl}|^2 \right) r \, dr. \quad (4.1)$$

For 3-D DNS conducted in this study, we consider a controlled initial condition as the combination of axisymmetric modes with $(j, l) = (0, \pm 1)$ and $\tilde{E}_{jl} = 5 \times 10^{-7}$ for each mode, which is most unstable, and other unstable non-axisymmetric modes with $(j, l) = (\pm 1, \pm 1)$ at a smaller amplitude with $\tilde{E}_{jl} = 5 \times 10^{-9}$ for each mode. These modes are computed from the 1-D local LSA and the non-axisymmetric modes are normalised to be out of phase, the case in which secondary instability can be promoted at the equilibrium state (i.e. axisymmetric Taylor vortices) reached by nonlinear saturation of the axisymmetric mode (see also Davey *et al.* 1968; Eagles 1974). Consideration of the non-axisymmetric modes with $j = \pm 1$ (i.e. $m = \pm 1$) is essential to allow the nonlinear energy transfer to modes with higher azimuthal wavenumber $|m| > 1$ and axial wavenumber jk with $|j| \geq 1$. For the analysis of secondary instability with the 2-D bi-global LSA presented in the following subsections, 2-D DNS are also conducted by considering the axisymmetric modes only (i.e. $M = 0$ and $N_\theta = 1$).

4.1. Nonlinear saturation to axisymmetric Taylor vortices

Figure 6(a) shows an example of the time evolution of the total energy $E(t)$ for case 1 and a few representative examples of the modal energy \hat{E}_{jl} for the axisymmetric mode with $(j, l) = (0, 1)$, the non-axisymmetric mode with $(j, l) = (1, 1)$ and the mean-flow distortion with $(j, l) = (0, 0)$. It is recalled that the indices j and l are from the azimuthal wavenumber $m_j = jm$ and axial wavenumber $k_l = lk$. At the initial stage, the perturbation energy is small enough and the total energy grows exponentially as $E(t) \sim \exp(2\text{Im}(\omega_{01})t)$, where ω_{01} is the growth rate of the most unstable axisymmetric mode (i.e. $j = 0$ and $l = 1$). A good agreement between the LSA prediction and DNS is clearly shown in figure 6(a) for the growth of the $m = 0$ and $m = 1$ modes at early stage. Once the energy of the axisymmetric mode increases and saturates, the flow reaches an equilibrium state featuring axisymmetric Taylor vortices as shown in figure 6(b).

In this saturation process, the mean-flow distortion also grows and its energy \hat{E}_{00} saturates. While the energies of the axisymmetric mode and mean-flow distortion remain constant at large t , the energy of the non-axisymmetric mode with $(j, l) = (1, 1)$ decays as the Taylor vortices appear. It is not shown here but other modes with higher m or k also decay as the Taylor vortices appear. Using the Taylor vortices at saturation as a new base state, the bi-global LSA can predict the decay of non-axisymmetric modes with the index $l = 1$ as we see a good agreement on the decay rate between the DNS and the bi-global LSA predictions. In figure 6(c), the total temperature $\Theta(r, z) = T_B + T$ at the equilibrium state is displayed. For case 1, thermal diffusion is moderate with $Pr = 1$ and thus the temperature perturbation T can grow and have an amplitude comparable to T_B at equilibrium. In this case, the total temperature Θ no longer varies linearly but is affected and mixed by the Taylor vortices; i.e. the temperature Θ increases (decreases) in the region where the direction of the velocity is upwards (downwards). The Taylor vortices in stratified fluids lead to baroclinicity with a radial temperature gradient; however, for case 1 with moderate $N = 1$ and $Re_i = 145$, the overturning of the temperature does not occur and it does not become secondarily unstable. Supplementary movie 1 available at <https://doi.org/10.1017/jfm.2025.261> demonstrates the nonlinear development of the Taylor vortices and perturbation through the saturation process. It is not shown here but with the same physical parameters of case 1, different sets of numerical parameters are tested (i.e. a higher-resolution case with $(N_r, N_\theta, N_z) = (120, 65, 65)$ and another case with a longer domain $L_z = 8\pi/k$ with resolution $(N_r, N_\theta, N_z) = (60, 33, 129)$). The results are found to be the same qualitatively with the appearance of axisymmetric Taylor vortices without secondary instability and quantitatively with insignificant differences in the energy growth curves.

4.2. Bi-global linear stability analysis and secondary instability

For the Taylor vortex flow, which is axisymmetric, we can explore its secondary instability by performing a 2-D bi-global LSA. To obtain the axisymmetric base state $\bar{\mathbf{Q}}(r, z) = (\bar{\mathbf{U}}(r, z), \bar{T}(r, z))$ for the bi-global LSA, 2-D DNS with $N_\theta = 1$ (i.e. $M = 0$) are conducted instead of 3-D DNS for computational efficiency. Another reason for using 2-D DNS is that the base state $\bar{\mathbf{Q}}$ does not become secondarily unstable but remains saturated, and thus we can use this steady and axially periodic base state in the bi-global LSA (see also Park *et al.* 2011). Figure 7 shows examples of the growth rates of the most unstable modes versus the Reynolds-number ratio $\mathcal{R}_c = Re_i/Re_{i,c}$. Results are computed from the 1-D local LSA (dashed lines) and 2-D bi-global LSA (solid lines). Highly non-axisymmetric modes not appearing in figure 7 are more stable than the modes shown in figure 7. For every 1-D case in figure 7, the axisymmetric mode with $m = 0$ becomes primarily unstable, as shown by black dashed lines. In both 1-D and 2-D LSA, the axial wavenumber $k = k_c$ of the axisymmetric mode at the onset of instability $\mathcal{R}_c = 1$. In the bi-global LSA, we use the Taylor vortices with axial wavenumber $k = k_c$, the value at the onset of instability $Re_i = Re_{i,c}$, and compute growth rates of non-axisymmetric modes with $m > 0$ by increasing \mathcal{R}_c . For $\mathcal{R}_c < 1$, growth rates of non-axisymmetric modes computed from the bi-global LSA are the same as those from the 1-D LSA since the axisymmetric Taylor vortices are not developed and the base state obtained from 2-D DNS is essentially cylindrical Couette flow (2.4). For the unstratified case with $N = 0$ in figure 7(a), the axisymmetric mode becomes unstable at $Re_{i,c} \simeq 131.6$. As the axisymmetric Taylor vortices appear for $Re_i > Re_{i,c}$, the growth rates of non-axisymmetric modes for $m \geq 1$ are attenuated by this new base state as shown by coloured solid lines in figure 7(a). In the presence of the Taylor vortices, growth rates of weakly non-axisymmetric modes for $1 \leq m \leq 4$ increase slowly

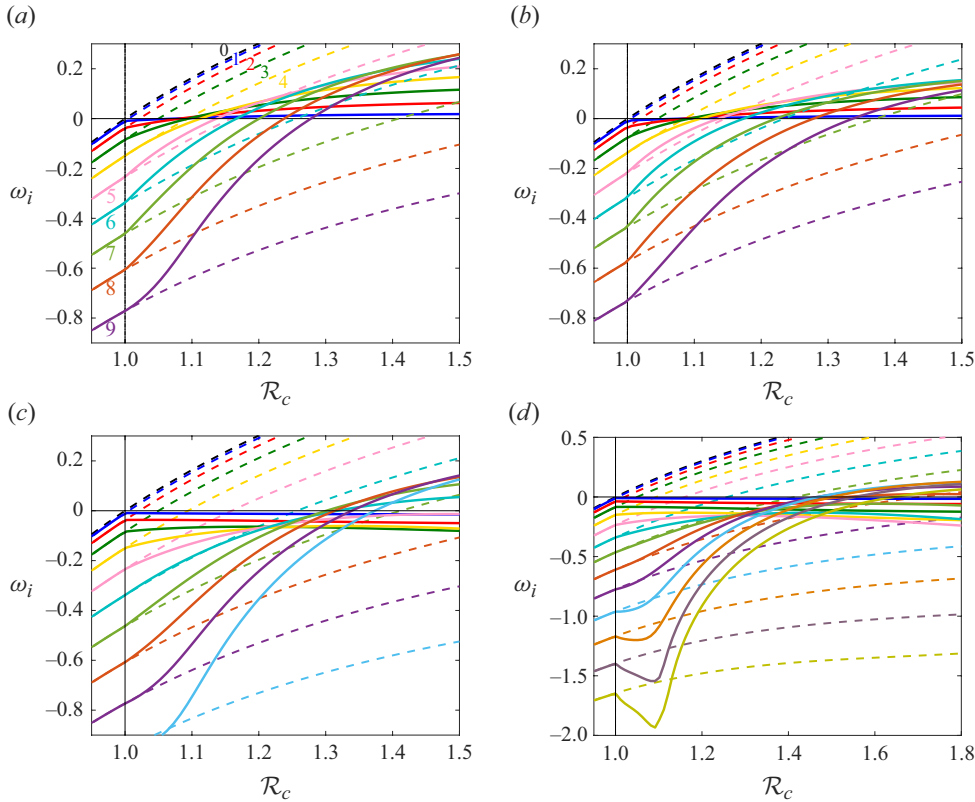


Figure 7. Growth-rate curves from 1-D LSA (dashed lines) and 2-D bi-global LSA (solid lines) for (a) unstratified case $N=0$ with numbers denoting m , (b) $(N, Pr) = (1, 1)$, (c) $(N, Pr) = (1, 0.01)$ and (d) $(N, Pr) = (1.5, 0.01)$. Black dashed lines denote the growth rate of the axisymmetric mode $m=0$ and other coloured curves in descending order (for $\mathcal{R}_c < 1$) denote the growth rate for $m=1$ and higher m .

with \mathcal{R}_c and the non-axisymmetric mode with $m=1$ becomes unstable at $\mathcal{R}_c = 1.075$ (i.e. $Re_i = Re_{i,2} \simeq 141.5$, where $Re_{i,2}$ denotes the secondary critical Reynolds number at which a non-axisymmetric mode becomes secondarily unstable). When $\mathcal{R}_c = 1.075$, the growth rates of highly non-axisymmetric modes increase faster with \mathcal{R}_c for the base flow case with Taylor vortices than the case with cylindrical Couette flow. This implies that highly non-axisymmetric modes are strongly promoted by the axisymmetric Taylor vortices for large \mathcal{R}_c . However, the $m=1$ mode is the second unstable mode and it is difficult to predict in advance which non-axisymmetric mode becomes the next dominant mode for $Re_i > Re_{i,2}$ as nonlinear interactions involving the growth of the $m=1$ mode will lead to a new non-axisymmetric base state.

Characteristics of secondary instability are similar for a stratified case with $(N, Pr) = (1, 1)$ in figure 7(b), the case where the axisymmetric mode becomes primarily unstable at a higher $Re_{i,c} \simeq 140.10$ and the non-axisymmetric mode with $m=1$ becomes secondarily unstable at a higher Reynolds-number ratio $\mathcal{R}_c = 1.085$ (i.e. $Re_{i,2} \simeq 152.1$) than the unstratified case. For a highly diffusive case with $Pr = 0.01$ in figure 7(c), characteristics of secondary instability change as weakly non-axisymmetric modes with $m=1$ and 2 are stabilised by the Taylor vortices while a highly non-axisymmetric mode with $m=7$ becomes secondarily unstable at $\mathcal{R}_c = 1.3$ (i.e. $Re_{i,2} = 171.31$). This implies that the onset of secondary instability is delayed by strong thermal diffusion at $Pr = 0.01$ and highly

non-axisymmetric modes become dominant while weakly non-axisymmetric modes are suppressed. The onset of secondary instability is further delayed as stratification becomes stronger with $N = 1.5$ as shown in figure 7(d), the case where the Taylor vortices become unstable by the $m = 9$ mode at a higher ratio with $\mathcal{R}_c = 1.466$ (i.e. $Re_{i,2} = 193.25$).

The prominence of highly non-axisymmetric modes, which become dominant over weakly non-axisymmetric modes with low m , can be understood by conducting an energetics analysis. Similar to (3.9), one can obtain an equation for the temporal evolution of perturbation energy from the linearised perturbation equations (A11)–(A15) as

$$\frac{\partial \bar{E}}{\partial t} = \mathcal{P}_{\bar{U}} + \mathcal{P}_{\bar{V}} + \mathcal{P}_{\bar{W}} + \mathcal{P}_{\bar{T}} - \mathcal{D}_K - \mathcal{D}_P, \quad (4.2)$$

where $\mathcal{P}_{\bar{U}, \bar{V}, \bar{W}, \bar{T}}$ are the production terms induced by axisymmetric Taylor vortices with $(\bar{U}, \bar{V}, \bar{W}, \bar{T})$ and $\mathcal{D}_{K,P}$ are the viscous and thermal dissipation terms, respectively, all of which are defined as follows:

$$\begin{aligned} \mathcal{P}_{\bar{U}} &= - \left\langle \frac{\partial \bar{U}}{\partial r} \bar{u}^2 + \frac{\bar{U}}{r} \bar{v}^2 + \frac{\partial \bar{U}}{\partial z} \bar{u} \bar{w} \right\rangle, & \mathcal{P}_{\bar{V}} &= - \left\langle \left(\frac{\partial \bar{V}}{\partial r} - \frac{\bar{V}}{r} \right) \bar{u} \bar{v} + \frac{\partial \bar{V}}{\partial z} \bar{v} \bar{w} \right\rangle, \\ \mathcal{P}_{\bar{W}} &= - \left\langle \frac{\partial \bar{W}}{\partial r} \bar{u} \bar{w} + \frac{\partial \bar{W}}{\partial z} \bar{w}^2 \right\rangle, & \mathcal{P}_{\bar{T}} &= -N^2 \left\langle \frac{\partial \bar{T}}{\partial r} \bar{u} \bar{T} + \frac{\partial \bar{T}}{\partial z} \bar{w} \bar{T} \right\rangle, \\ \mathcal{D}_K &= \frac{1}{Re} \langle \nabla \bar{\mathbf{u}} : \nabla \bar{\mathbf{u}} \rangle, & \mathcal{D}_P &= \frac{N^2}{RePr} \langle \nabla \bar{T} : \nabla \bar{T} \rangle. \end{aligned} \quad (4.3)$$

We note that the dissipation terms $\mathcal{D}_{K,P}$ are always positive and play a stabilising role while the production terms $\mathcal{P}_{\bar{U}, \bar{V}, \bar{W}, \bar{T}}$ are not necessarily positive as they depend on the correlation between the base state $(\bar{U}, \bar{V}, \bar{W}, \bar{T})$ and perturbation variables $(\bar{u}, \bar{v}, \bar{w}, \bar{T})$. Applying the normal mode (2.29) to (4.2) and considering the normalisation $\hat{E}_m = 1$, where \hat{E}_m is the modal energy defined as

$$\hat{E}_m = \left\langle |\hat{u}_m|^2 + |\hat{b}_m|^2 + |\hat{w}_m|^2 + N^2 |\hat{T}_m|^2 \right\rangle_{rz}, \quad \langle \hat{\mathbf{X}}_m \rangle_{rz} = \int_0^{L_z} \int_1^{1/\eta} \hat{\mathbf{X}}_m r \, dr \, dz, \quad (4.4)$$

we obtain the following relation between the growth rate $\omega_{m,i}$ and the modal contribution terms:

$$\omega_{m,i} = \hat{\mathcal{P}}_{m,\bar{U}} + \hat{\mathcal{P}}_{m,\bar{V}} + \hat{\mathcal{P}}_{m,\bar{W}} + \hat{\mathcal{P}}_{m,\bar{T}} - \hat{\mathcal{D}}_{m,K} - \hat{\mathcal{D}}_{m,P}, \quad (4.5)$$

where

$$\begin{aligned} \hat{\mathcal{P}}_{m,\bar{U}} &= - \left\langle \frac{\partial \bar{U}}{\partial r} |\hat{u}_m|^2 + \frac{\bar{U}}{r} |\hat{v}_m|^2 + \frac{\partial \bar{U}}{\partial z} \left(\frac{\hat{u}_m^* \hat{w}_m + \hat{u}_m \hat{w}_m^*}{2} \right) \right\rangle_{rz}, \\ \hat{\mathcal{P}}_{m,\bar{V}} &= - \left\langle \left(\frac{\partial \bar{V}}{\partial r} - \frac{\bar{V}}{r} \right) \left(\frac{\hat{u}_m^* \hat{v}_m + \hat{u}_m \hat{v}_m^*}{2} \right) + \frac{\partial \bar{V}}{\partial z} \left(\frac{\hat{v}_m^* \hat{w}_m + \hat{v}_m \hat{w}_m^*}{2} \right) \right\rangle_{rz}, \\ \hat{\mathcal{P}}_{m,\bar{W}} &= - \left\langle \frac{\partial \bar{W}}{\partial r} \left(\frac{\hat{u}_m^* \hat{w}_m + \hat{u}_m \hat{w}_m^*}{2} \right) + \frac{\partial \bar{W}}{\partial z} |\hat{w}_m|^2 \right\rangle_{rz}, \\ \hat{\mathcal{P}}_{m,\bar{T}} &= -N^2 \left\langle \frac{\partial \bar{T}}{\partial r} \left(\frac{\hat{u}_m^* \hat{T}_m + \hat{u}_m \hat{T}_m^*}{2} \right) + \frac{\partial \bar{T}}{\partial z} \left(\frac{\hat{w}_m^* \hat{T}_m + \hat{w}_m \hat{T}_m^*}{2} \right) \right\rangle_{rz}, \\ \hat{\mathcal{D}}_{m,K} &= \frac{1}{Re} \langle \hat{\mathbf{v}}_m \hat{\mathbf{u}}_m : \hat{\mathbf{v}}_m \hat{\mathbf{u}}_m \rangle_{rz}, & \hat{\mathcal{D}}_{m,P} &= \frac{N^2}{RePr} \langle \hat{\mathbf{v}}_m \hat{T}_m : \hat{\mathbf{v}}_m \hat{T}_m \rangle_{rz}. \end{aligned} \quad (4.6)$$

Re_i	N	Pr	m	Case	$\omega_{m,i}$	$\hat{\mathcal{P}}_{m,\bar{U}}$	$\hat{\mathcal{P}}_{m,\bar{V}}$	$\hat{\mathcal{P}}_{m,\bar{W}}$	$\hat{\mathcal{P}}_{m,\bar{T}}$	$\hat{\mathcal{D}}_{m,K}$	$\hat{\mathcal{D}}_{m,P}$	The sum (4.5)
200	1	0.01	0	1-D LSA	0.6274	0	1.5854	0	0	0.9577	0.0003	0.6273
200	1	0.01	1	1-D LSA	0.6165	0	1.5821	0	0	0.9654	0.0004	0.6164
200	1	0.01	1	2-D LSA	-0.0147	-0.0005	1.1594	0.0030	0.0000	1.1764	0.0005	-0.0150
200	1	0.01	5	2-D LSA	-0.0134	0.0112	1.2137	-0.0219	0.0000	1.2121	0.0046	-0.0136
200	1	0.01	9	2-D LSA	0.1525	0.0335	1.4639	-0.0641	0.0000	1.2700	0.0110	0.1522
200	1	0.01	13	2-D LSA	-0.0303	0.0371	1.4953	-0.1295	0.0000	1.4202	0.0133	-0.0306
200	1	1	0	1-D LSA	0.5441	0	1.5699	0	0	1.0143	0.0115	0.5441
200	1	1	1	1-D LSA	0.5346	0	1.5677	0	0	1.0213	0.0119	0.5345
200	1	1	1	2-D LSA	0.0105	0.0008	1.1757	0.0018	0.0269	1.1470	0.0479	0.0103
200	1	1	5	2-D LSA	0.1336	0.0147	1.3567	-0.0086	0.0192	1.2128	0.0360	0.1334
200	1	1	9	2-D LSA	0.0736	0.0259	1.4480	-0.0430	0.0112	1.3309	0.0377	0.0734
200	1	1	13	2-D LSA	-0.1690	0.0267	1.4451	-0.0981	0.0054	1.5029	0.0453	-0.1692

Table 3. Growth rates $\omega_{m,i}$ and contribution terms computed from 1-D local LSA and 2-D bi-global LSA for $(Re_i, N, Pr) = (200, 1, 0.01)$ and $(Re_i, N, Pr) = (200, 1, 1)$.

Examples of the growth rate ω_i and instability contribution terms (4.6) computed from the eigenfunction $\hat{\mathbf{q}}_m$ are presented in table 3. In the table, the growth rate $\omega_{m,i}$ computed from the eigenvalue problems (2.27) and (2.30) and the sum on the right-hand side of (4.5), which is obtained by integrating the eigenfunction computed from either (2.27) for 1-D LSA cases or (2.30) for 2-D LSA cases, are in good agreement with a very small difference of $O(10^{-4})$. For 1-D LSA cases in which the base flow is cylindrical Couette flow, the axisymmetric mode with $m = 0$ is most unstable due to the largest production $\hat{\mathcal{P}}_{m,\bar{V}}$ and the least total dissipation $\hat{\mathcal{D}}_m = \hat{\mathcal{D}}_{m,K} + \hat{\mathcal{D}}_{m,P}$. This applies to both cases with $Pr = 0.01$ and $Pr = 1$ although the thermal dissipation $\hat{\mathcal{D}}_{m,P}$ is small when Pr is small. As m increases, the production $\hat{\mathcal{P}}_{m,\bar{V}}$ decreases while the dissipation $\hat{\mathcal{D}}_m$ increases, which leads to the decrease of the growth rate. For $m = 1$, we compare the 1-D LSA cases against the 2-D LSA cases where the base flow is 2-D axisymmetric Taylor vortices. It is clearly shown that the growth rate decreases as the flow becomes 2-D with decrease in the total production term $\hat{\mathcal{P}}_m = \hat{\mathcal{P}}_{m,\bar{U}} + \hat{\mathcal{P}}_{m,\bar{V}} + \hat{\mathcal{P}}_{m,\bar{W}} + \hat{\mathcal{P}}_{m,\bar{T}}$ and increase in the total dissipation $\hat{\mathcal{D}}_m$. While other production terms such as $\hat{\mathcal{P}}_{m,\bar{U}}$, $\hat{\mathcal{P}}_{m,\bar{W}}$ and $\hat{\mathcal{P}}_{m,\bar{T}}$ appear for 2-D cases due to the velocity and temperature gradients of the Taylor vortices in the radial and axial directions (see also figure 6*b,c*), their contribution to the growth rate is smaller than the contribution from the azimuthal velocity \bar{V} (i.e. $\hat{\mathcal{P}}_{m,\bar{V}}$). What is noteworthy in secondary instability of axisymmetric Taylor vortices is that the total dissipation $\hat{\mathcal{D}}_m$ increases monotonically with m while the total production $\hat{\mathcal{P}}_m$ increases and then decreases as m increases.

Figure 8(*a,b*) demonstrates behaviours of the growth rate $\omega_{m,i}$, production $\hat{\mathcal{P}}_m$ and dissipation $\hat{\mathcal{D}}_m$ with varying m for different Pr at $(Re_i, N) = (200, 1)$. Except for $Pr = 0.01$, the growth rate $\omega_{m,i}$ increases first and then decreases as m increases (figure 8*a*). This is due to the fact that the production $\hat{\mathcal{P}}_m$ increases only for small m and decreases as m increases further while the dissipation $\hat{\mathcal{D}}_m$ increases exponentially with m (figure 8*b*). This results in the growth rate $\omega_{m,i}$ being positive only in a finite range of m . The growth rates for $Pr = 10^{-4}$ and $Pr = 10^{-6}$ are very similar to each other and are higher than $\omega_{m,i}$ for $Pr = 1$. The growth rate behaviour for $Pr = 0.01$ is more complicated as $\omega_{m,i}$ is negative for $m \leq 5$ before it shows a similar increasing/decreasing trend. Only highly non-axisymmetric modes in the range $6 \leq m \leq 12$ are secondarily unstable for $Pr = 0.01$ while

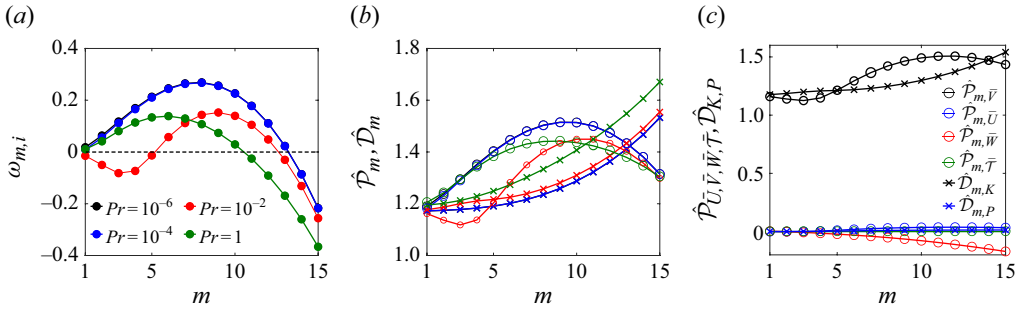


Figure 8. (a,b) Growth rate $\omega_{m,i}$ (filled circles in a), production \hat{P}_m (open circles in b) and dissipation \hat{D}_m (crosses in b) versus azimuthal wavenumber m for different Pr : $Pr = 10^{-6}$ (black), 10^{-4} (blue), 0.01 (red) and 1 (green) at $(Re_i, N) = (200, 1)$. (c) Production and dissipation terms versus m for $(Re_i, N, Pr) = (200, 1, 0.01)$.

non-axisymmetric modes for other Pr cases are unstable in broader ranges of m such as $1 \leq m \leq 10$ for $Pr = 1$ and $1 \leq m \leq 13$ for $Pr = 10^{-4}$ and 10^{-6} . This implies that a highly non-axisymmetric flow pattern, as further discussed in the next subsection, can appear for $Pr = 0.01$ by secondary instability of Taylor vortices. Figure 8(c) describes variations of all the production and dissipation terms with m at $(Re_i, N, Pr) = (200, 1, 0.01)$. The dominant production and dissipation terms are $\hat{P}_{\bar{v}}$ and \hat{D}_K while other terms are small. The production term $\hat{P}_{\bar{w}}$ becomes negative as $m > 1$ increases implying the stabilising role of the axial velocity \bar{w} .

Figure 9 details how the growth rate, production and dissipation vary with Pr for various non-axisymmetric modes at $Re_i = 200$ and $N = 1$. In figure 9(a), we see that, for low $m \leq 7$, the growth rate $\omega_{m,i}$ decreases as Pr decreases from $Pr = 1$ and then it increases as Pr further decreases from $Pr = 10^{-1}$ to 10^{-2} . For high $m \geq 8$, the growth rate increases monotonically as Pr decreases. Such behaviours are similar for the total production term \hat{P}_m while the dissipation term \hat{D}_m decreases overall monotonically as Pr decreases, as shown in figure 9(b). As revealed in figure 8(c), the dominant contributions to the production and dissipation come from $\hat{P}_{m,\bar{v}}$ and $\hat{D}_{m,K}$, respectively, which have the magnitude of $O(1)$ (figure 9c). The Pr behaviour of $\hat{P}_{m,\bar{v}}$ is similar to that of the total production \hat{P}_m , which drives the growth rate. Although it is not straightforward to delineate the Pr tendency on which non-axisymmetric mode becomes most unstable, one can infer from figure 9(c) that highly non-axisymmetric modes overall contribute to the secondary instability via its interaction with the azimuthal velocity \bar{v} when Pr is sufficiently low as $Pr < 10^{-2}$, while the behaviour is more complicated in the range $10^{-2} < Pr < 1$. In figure 9(d), we describe other contribution terms $\hat{P}_{m,\bar{u}}$, $\hat{P}_{m,\bar{w}}$ and $\hat{D}_{m,P}$, which are minor with a magnitude of $O(0.1)$ or less. The production $\hat{P}_{m,\bar{u}}$ is overall positive except for $m = 1$ around $Pr = 10^{-2}$ and behaves similar to $\hat{P}_{m,\bar{v}}$ while the contribution $\hat{P}_{m,\bar{w}}$ is overall negative except for the case with $m = 1$, which is positive, and overall decreases as Pr decreases. As can be inferred from the expression in (4.6), thermal dissipation $\hat{D}_{m,P}$ overall decreases to zero as Pr decreases.

Figure 10 displays different neutral stability curves obtained from the 1-D local LSA (solid lines) and 2-D bi-global LSA (dashed lines) to show how the critical Reynolds numbers $Re_{i,c}$ and $Re_{i,2}$ vary with the Prandtl number Pr or the Brunt–Väisälä frequency N . For $(N, Pr) = (1, 1)$ in figure 10(a), primary centrifugal instability by

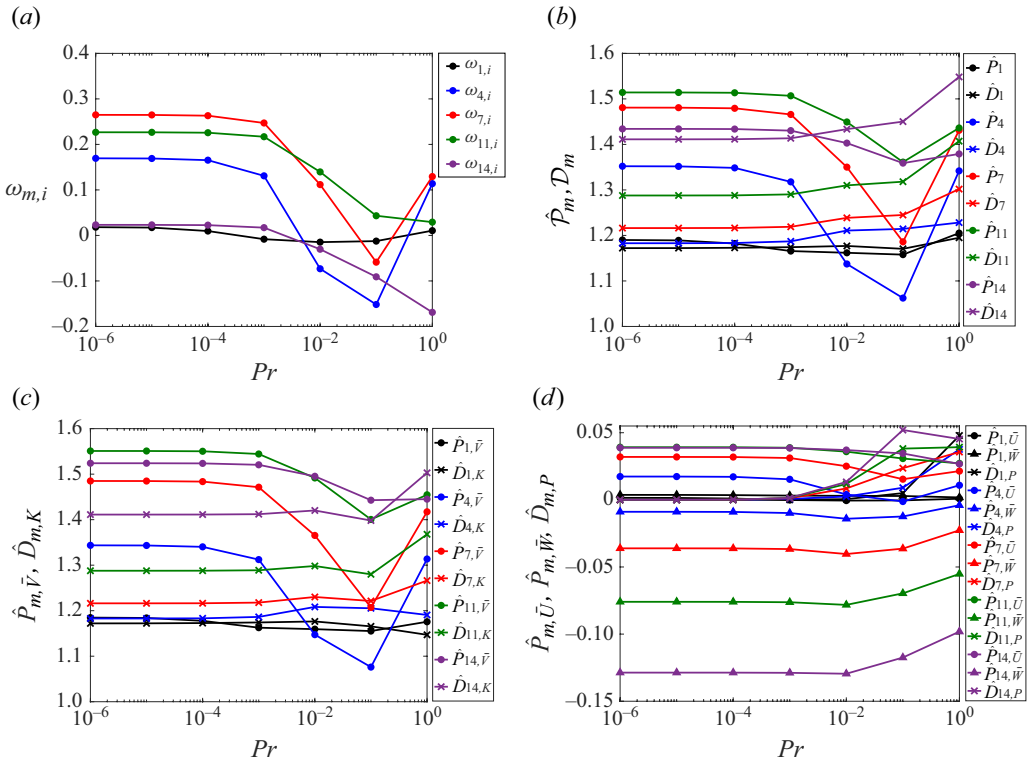


Figure 9. Variations with the Prandtl number Pr for (a) the growth rate $\omega_{m,i}$, (b) the total production \hat{P}_m and dissipation \hat{D}_m , (c) the dominant production term $\hat{P}_{m, \bar{V}}$ and dissipation term $\hat{D}_{m, K}$ and (d) other production terms $\hat{P}_{m, \bar{U}}, \hat{P}_{m, \bar{W}}$ and dissipation term $\hat{D}_{m, P}$ for different $m = 1, 4, 7, 11$ and 14 at $Re_i = 200$ and $N = 1$.

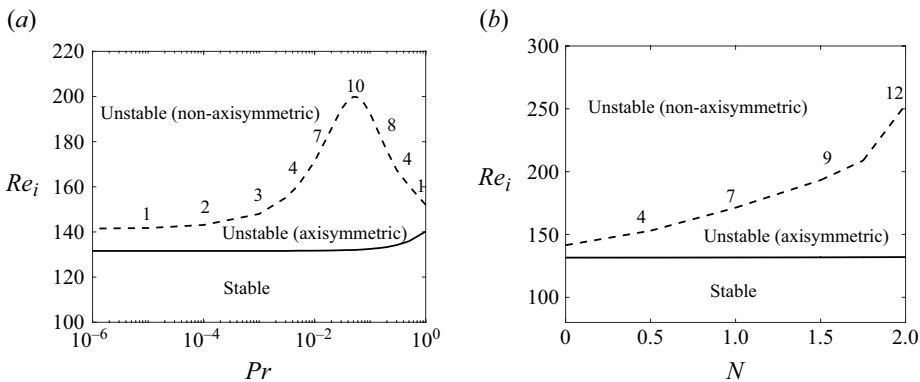


Figure 10. Neutral stability curves from the 1-D LSA of the axisymmetric mode $m = 0$ (solid lines denoting $Re_{i,c}$) and bi-global LSA of the non-axisymmetric modes (dashed lines denoting $Re_{i,2}$) for (a) $N = 1$ and (b) $Pr = 0.01$. The numbers above the dashed lines indicate the azimuthal wavenumbers of the non-axisymmetric mode which becomes secondarily unstable.

an axisymmetric mode occurs at $Re_{i,c} = 140.2$ while secondary instability occurs at $Re_{i,2} = 152.0$ by a non-axisymmetric mode with $m = 1$. At $N = 1$, the critical Reynolds number $Re_{i,c}$ decreases monotonically as Pr decreases while the secondary critical

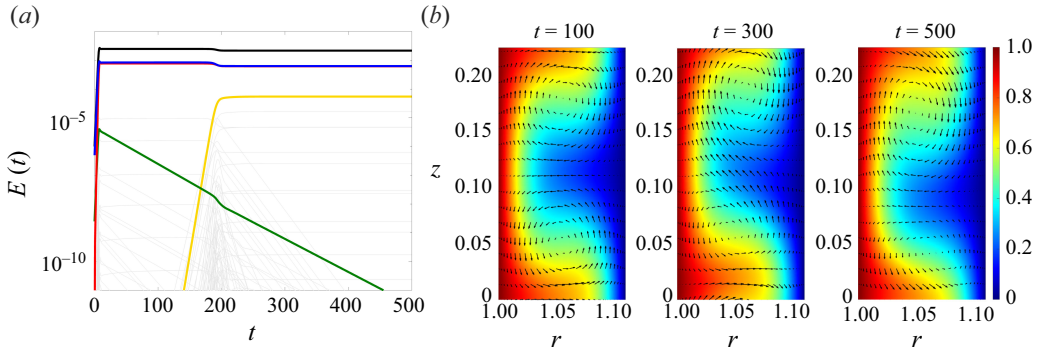


Figure 11. (a) Temporal evolution of the total energy $E(t)$ (black) and modal energy components \tilde{E}_{jl} for case 2: \tilde{E}_{00} (red), \tilde{E}_{01} (blue), \tilde{E}_{11} (green), \tilde{E}_{91} (yellow), and other energy components denoted by grey lines. (b) The corresponding instantaneous velocity profiles at different times on the plane (r, z) at $\theta = 0$. The contours denote the azimuthal velocity $U_\theta(r, z)$ and the vector plot denotes the transverse velocity field (U_r, U_z) .

Reynolds number $Re_{i,2}$ increases as Pr decreases from $Pr = 1$ to $Pr = 0.06$ and then $Re_{i,2}$ decreases monotonically from the peak at $Pr = 0.06$ as Pr further decreases. It is noteworthy that, in the range $10^{-3} < Pr < 1$, the secondary instability is triggered by highly non-axisymmetric modes with $m \geq 4$; thus for $Re_i > Re_{i,2}$, we expect to observe highly non-axisymmetric flow patterns in this range of Pr . This highly non-axisymmetric pattern is further discussed in the following subsection. In the range $Pr \leq 10^{-3}$, the critical Reynolds numbers $Re_{i,c}$ and $Re_{i,2}$ approach those of the unstratified case at $N = 0$ (i.e. $Re_{i,c} = 131.6$ and $Re_{i,2} = 141.5$), the case with secondary instability triggered by a non-axisymmetric mode with $m = 1$. At $Pr = 0.01$, it is shown in figure 10(b) that the critical Reynolds number $Re_{i,c}$ does not change significantly in the range $0 \leq N \leq 2$ (e.g. $Re_{i,c} = 131.6$ at $N = 0$ and $Re_{i,c} = 132.0$ at $N = 2$) while the secondary critical Reynolds number $Re_{i,2}$ increases monotonically with N . The corresponding azimuthal wavenumber of the non-axisymmetric mode, which triggers secondary instability, also increases with N .

Neutral stability curves in figure 10 delineate the regimes of axisymmetric and non-axisymmetric flow patterns in the parameter space (Re_i, Pr) or (Re_i, N) . The results are obtained by 1-D and 2-D LSA and we discuss in the next subsection about nonlinear simulation results how flow patterns change from axisymmetric Taylor vortices to non-axisymmetric wavy vortices via secondary instability or how the flow transitions to a chaotic and irregular state, a precursor stage prior to turbulence.

4.3. Transition of flow patterns

We now consider case 2 at $(Re_i, N, Pr) = (200, 1, 0.01)$, a case where the axisymmetric Taylor vortices become secondarily unstable by highly non-axisymmetric modes (see also figures 7c and 10a). The perturbation energy plot in figure 11(a) shows that the axisymmetric mode becomes unstable and saturates quickly to the state of axisymmetric Taylor vortices (e.g. figure 11b at $t = 100$). At this first saturation state, the energies of weakly non-axisymmetric modes like the $m = 1$ mode (green line in figure 11a) decay exponentially. In contrast, highly non-axisymmetric modes like the $m = 9$ mode (yellow line in figure 11a) become unstable as the axisymmetric Taylor vortices sustain and their

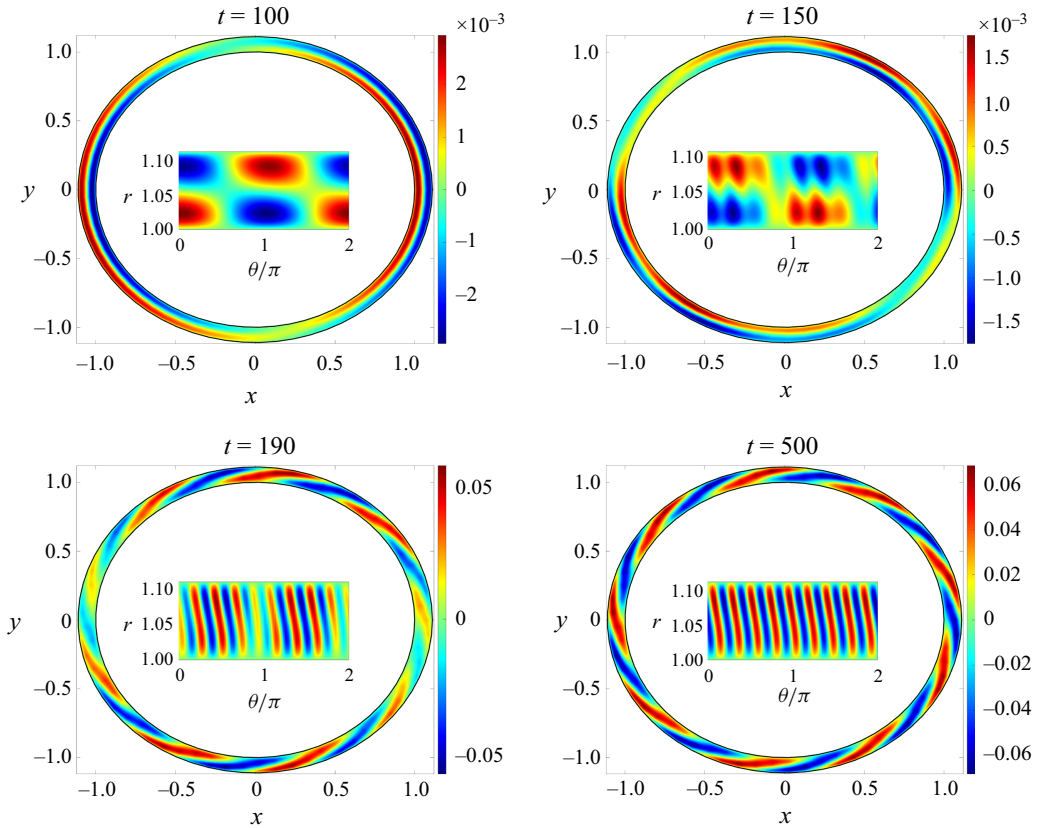


Figure 12. Time evolution of the vertical velocity u_z in the (x, y) plane at $z = 0$ for case 2.

amplitudes become comparable to that of the axisymmetric mode as $t > 200$. The flow reaches a second saturation state in which the Taylor vortices start to oscillate vertically (figure 11*b* and supplementary movie 2) and become non-axisymmetric. The transition at which non-axisymmetric modes become dominant is clearly illustrated by the vertical velocity $u_z(x, y)$ plot for different time t (figure 12 and supplementary movie 3). The most energetic non-axisymmetric mode with $m = 1$ loses its energy at the first transition stage (e.g. u_z at $t = 100$) while other non-axisymmetric modes with higher m gain their energies and become comparable in the transition stage $150 < t < 200$. Weakly and highly non-axisymmetric modes compete during the transition (e.g. u_z at $t = 150$ and 190) and after $t > 200$, the non-axisymmetric mode with $m = 9$ becomes the second dominant mode after the axisymmetric mode $m = 0$ forming the wavy Taylor vortices. This non-axisymmetric pattern in u_z has a maximum amplitude around the centreline between the two cylinders and is different from the feature of SRI, which is triggered by two out-of-phase inertia-gravity waves confined near the two cylinders and has maxima near the cylinders (Park & Billant 2013; Park *et al.* 2017). Contours of the azimuthal vorticity $\omega_\theta = \partial u_r / \partial z - \partial u_z / \partial r$ in figure 13(*a*) clearly show the axisymmetric Taylor vortices at $t = 100$ as the first saturation state and non-axisymmetric wavy Taylor vortices as the second saturation state. Various modal energies of the perturbation are expected to either saturate or decay after $t > 500$ and thus non-axisymmetric Taylor vortices sustain for large t .

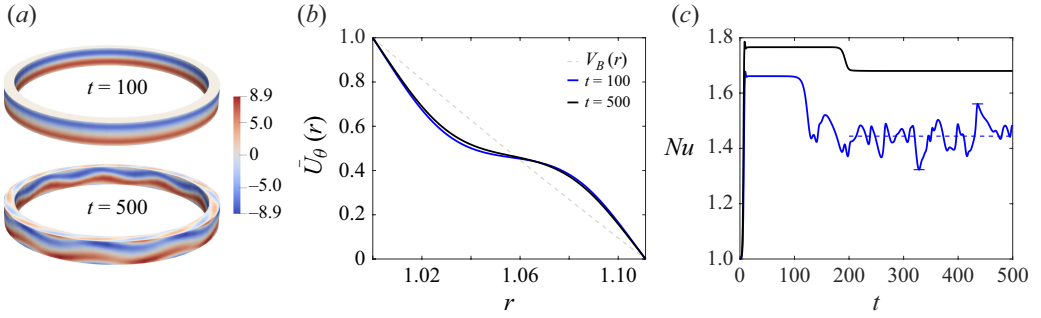


Figure 13. (a) Contours of the azimuthal vorticity ω_θ at the boundary surfaces for case 2. (b) Profiles of the averaged velocity $\bar{U}_\theta(r)$ and cylindrical Couette flow $V_B(r)$ for case 2. (c) Nusselt number Nu as a function of time t for case 2 (black) and case 3 (blue).

Figure 13(b) shows profiles of the total averaged azimuthal velocity $\bar{U}_\theta(r, t) = V_B(r) + \bar{v}_{00}(r, t)$, the latter which is the azimuthal velocity of the mean-flow distortion denoting the azimuthal perturbation velocity averaged in the directions θ and z . Compared with the profile of \bar{U}_θ at $t = 100$ for the axisymmetric Taylor vortices at the first saturation, the distortion in the azimuthal velocity is reduced for non-axisymmetric wavy Taylor vortices at the second saturation. The reduced distortion in mean flow implies the reduction in the velocity gradient at the inner cylinder and the corresponding torque applied at the inner cylinder. Following Martínez Arias (2015), we define an axially averaged non-dimensional torque G at the inner cylinder as

$$G = \left(\frac{\eta Re_i}{1 - \eta} \right) \frac{1}{2\pi L_z} \int_0^{2\pi} \int_0^{L_z} \left(\frac{U_\theta}{r} - \frac{\partial U_\theta}{\partial r} \right) \bigg|_{r=1} d\theta dz, \quad (4.7)$$

which gives the laminar torque G_{lam} for cylindrical Couette flow $U_\theta = V_B(r)$ as

$$G_{\text{lam}} = \frac{2\eta(1 - \mu)Re_i}{(1 + \eta)(1 - \eta)^2}. \quad (4.8)$$

We also define the Nusselt number Nu as $Nu = G/G_{\text{lam}}$, which is the ratio between the transverse convective transport of angular velocity and the molecular transport of angular velocity as a measure of the non-dimensional angular momentum transfer (Dubrulle & Hersant 2002; Eckhardt *et al.* 2007; Martínez Arias 2015). Figure 13(c) shows how the Nusselt number Nu changes over time for case 2 (black line). Compared with the axisymmetric Taylor vortices in the range $50 \leq t \leq 150$ having a constant $Nu = 1.77$ during the first saturation process, the wavy Taylor vortices at the second saturation in the range $t > 200$ have a lower $Nu = 1.68$. This implies that the non-axisymmetric Taylor vortices after secondary instability lead to reduced angular momentum transfer compared with the axisymmetric Taylor vortices after primary centrifugal instability.

Case 3 with $(N, Pr) = (1, 1)$ considers the Reynolds number $Re_i = 200$ at the ratio $\mathcal{R}_2 = Re_i/Re_{i,2} = 1.316$, which is larger than the ratio $\mathcal{R}_2 = 1.168$ in case 2. In this case, it is observed that the secondary instability bypasses the saturation but leads to an irregular fluctuation as shown by the temporal variation of the Nusselt number Nu in figure 13(c) and modal energies of perturbation in figure 14(a). Primary centrifugal instability breaks down as $t > 100$ where other non-axisymmetric modes including the mode with $m = 1$ become dominant with strong nonlinear modal interaction. For case 3, the most energetic mode varies over time and the flow exhibits a rather chaotic temporal fluctuation as shown by the energy evolution in figure 14(a) and by the velocity and temperature fields in the

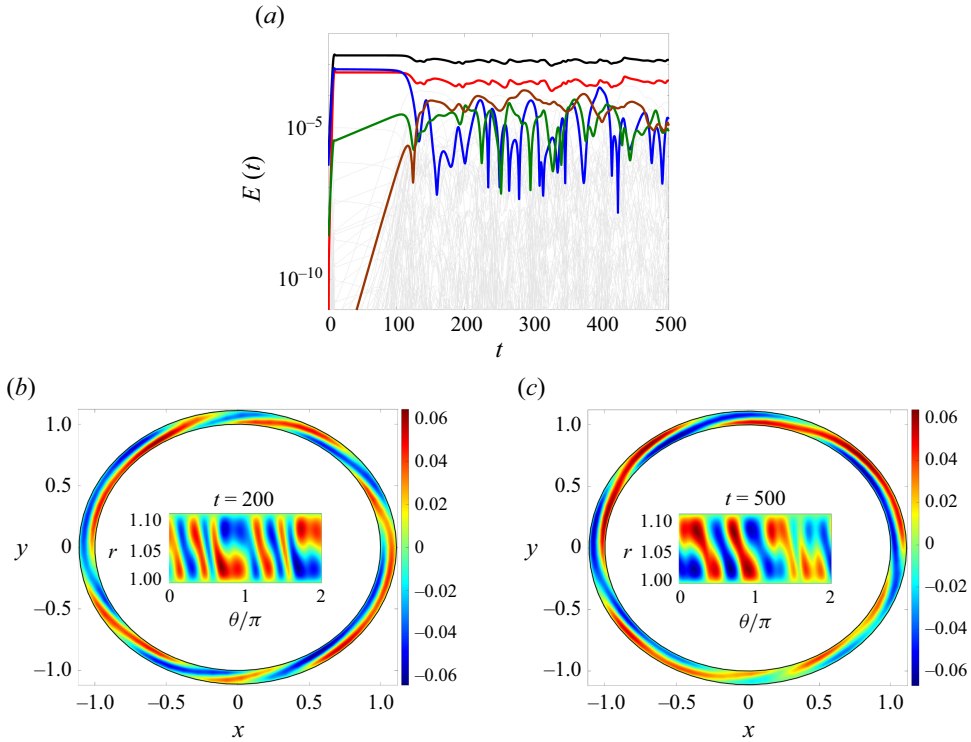


Figure 14. (a) Temporal evolution of the total energy $E(t)$ (black) and modal energy components \tilde{E}_{jl} for case 3: \tilde{E}_{00} (red), \tilde{E}_{01} (blue), \tilde{E}_{11} (green), \tilde{E}_{41} (brown), and other energy components denoted by grey lines. Corresponding instantaneous velocity field $u_z(x, y)$ at $z = 0$ at (b) $t = 200$ and (c) $t = 500$.

(r, z) plane in supplementary movies 4 and 5. Although this irregular flow state does not show a small length-scale structure (see also figure 14b and supplementary movie 6), the levels of the modal energies of large-wavenumber modes are not negligible and turbulence is expected to occur for $(N, Pr) = (1, 1)$ at high Reynolds number $Re_i > 200$, the range to be further explored in a future study. The Prandtl number $Pr = 1$ is not small and the temperature perturbation T is comparable with the base temperature T_B . Therefore, the fluctuation in the total temperature $\Theta = T_B + T$ induced by the velocity fluctuation is visible as shown in figure 15(a) although the overturning of temperature, which is a potential source of baroclinic instability, does not occur. Chaotic fluctuation of the temperature Θ after $t > 100$ is also clearly shown in the spatio-temporal diagram measured near the mid-point at $r = 1.05$ (figure 15b).

Figure 16(a) shows how the Nusselt number Nu changes with the Reynolds number Re_i for different sets of (N, Pr) : $(1, 1)$ (blue), $(1, 0.01)$ (red), $(1, 10^{-4})$ (green) and the unstratified case with $N = 0$ (black). The Nusselt number Nu is computed at the saturation state of the axisymmetric Taylor vortices (filled circles), which are computed through 3-D DNS with a numerical resolution the same as that in case 1, or for non-axisymmetric wavy vortices at the second saturation (filled squares) computed by 3-D DNS with a numerical resolution the same as that in case 2. For the flow in which its instability does not saturate and Nu fluctuates like case 3, open squares with error bars are used to indicate the mean, minimum and maximum Nu averaged in the time interval of fluctuation (see e.g. figure 13c). In these cases with fluctuations, the same numerical resolution as in

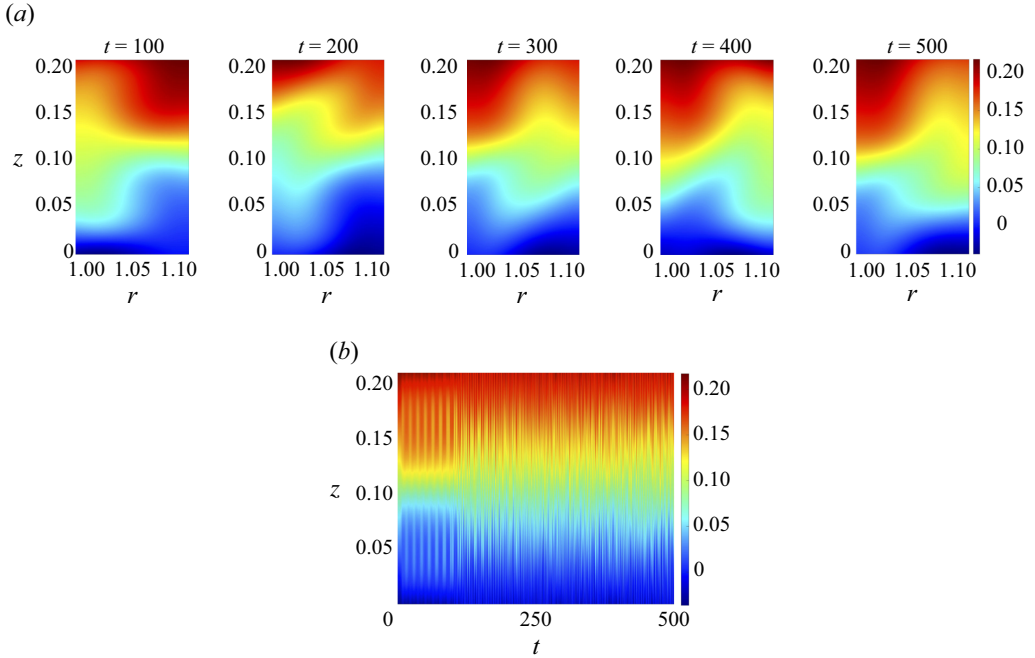


Figure 15. (a) Evolution of the total temperature $\Theta(r, z)$ at $\theta = 0$ for case 3. (b) Corresponding spatio-temporal diagram of $\Theta(t, z)$ measured at $r = 1.05$ and $\theta = 0$.

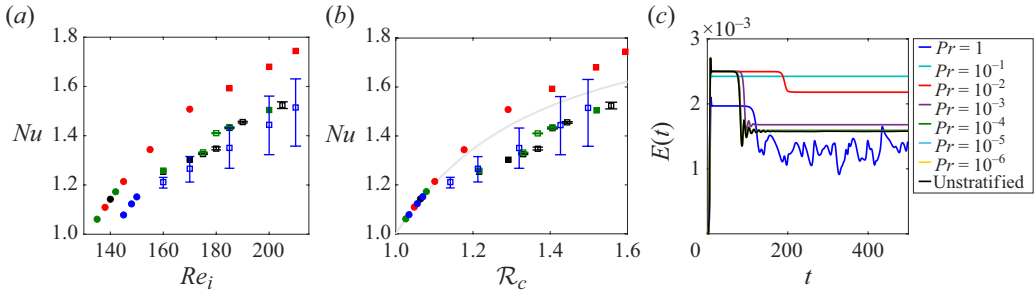


Figure 16. (a) Nusselt number Nu versus Reynolds number Re_i for $N = 0$ (black), $(N, Pr) = (1, 1)$ (blue), $(N, Pr) = (1, 0.01)$ (red) and $(N, Pr) = (1, 10^{-4})$ (green). Filled circles and squares indicate Nu for the axisymmetric Taylor vortices and non-axisymmetric wavy vortices at saturation, respectively. Open squares with error bars indicate statistically averaged Nu and the minimum and maximum of Nu in the time interval considered (see also figure 13c). (b) Nusselt number Nu same as (a) but over the rescaled Reynolds-number ratio R_c . The grey line indicates the Nusselt number from (4.9). (c) Temporal evolution of the total energy $E(t)$ for different Pr at $Re_i = 200$ and $N = 1$. Black line denotes the unstratified case with $N = 0$.

case 3 is used. It is clearly shown that Nu for cases with the axisymmetric Taylor vortices increases fast with Re_i and it increases slowly down as secondary instability occurs. The increasing trend of the Nusselt number Nu is similar for unstratified cases with $N = 0$ and stratified cases with $(N, Pr) = (1, 10^{-4})$. For both sets, secondary instability leading to a fluctuating flow state appears for $Re_i > 160$ and there is a jump in Nu around $Re_i = 180$. The Nusselt number Nu continues to increase similarly for both as Re_i increases further for $Re_i > 180$. For the cases with $(N, Pr) = (1, 0.01)$, the Nusselt number Nu is higher

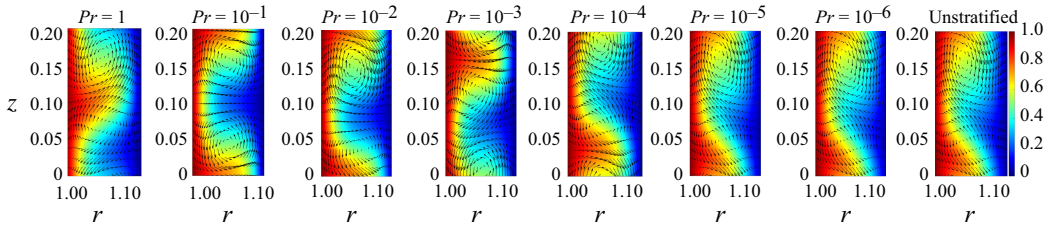


Figure 17. Instantaneous velocity contours for U_θ and vector plots for the transverse velocity field (U_r , U_z) on the plane (r, z) for different Pr at $t = 500$, $\theta = 0$, $Re_i = 200$ and $N = 1$. The rightmost panel corresponds to the unstratified case with $N = 0$.

than for other cases as secondary instability occurs at a later stage as $Re_{i,2} = 171.31$ for $Pr = 0.01$. Up to $Re_i = 210$, the breakdown of secondary instability is not observed for $Pr = 0.01$. Unlike other cases with critical Reynolds numbers $Re_{i,c} = 131.6$ – 131.7 , the centrifugal instability for $(N, Pr) = (1, 1)$ occurs at a higher $Re_{i,c} = 140.2$ and thus Nu in this case is smaller than for other cases at the same Re_i . Although the onset of primary centrifugal instability is delayed for $(N, Pr) = (1, 1)$, it is found that the breakdown of instability occurs early and the fluctuation in Nu is larger than in other cases.

For a better comparison among the cases, we display in figure 16(b) the same Nu against the Reynolds-number ratio $\mathcal{R}_c = Re_i / Re_{i,c}$. For the axisymmetric Taylor vortices, DiPrima *et al.* (1984) proposed the following scaling law for Nu as a function of the ratio \mathcal{R}_c :

$$Nu = 1 + A \left(1 - \frac{1}{\mathcal{R}_c^2} \right) + B \left(1 - \frac{1}{\mathcal{R}_c^2} \right)^2, \quad (4.9)$$

where $A = 1.246$ and $B = -0.37$ are the constants for $\eta = 0.9$ according to DiPrima *et al.* (1984). It is clearly shown in figure 16(b) that Nu for every case agrees well with the scaling law (4.9) in the range $\mathcal{R}_c \leq 1.1$ where the axisymmetric Taylor vortices are present. This implies that Nu for the Taylor vortices, which are induced by primary centrifugal instability, is not strongly influenced by Pr . When the flow is secondarily unstable or chaotic, the cases with $(N, Pr) = (1, 0.01)$ for which secondary instability appears late as $\mathcal{R}_c > 1.3$ have higher Nu than the scaling law (4.9) while other cases for which secondary instability appears early as $\mathcal{R}_c > 1.1$ have lower Nu than the proposed scaling (4.9). This implies that the angular momentum transport represented by Nu depends on Pr once the flow becomes secondarily unstable or chaotic. However, as figure 16(a,b) only considers $N = 1$, more detailed investigations are required to confirm the relation between Nu and Pr in a wider parameter space of (N, Re_i) , an important topic to be further studied in the future to unravel the physics of turbulent angular momentum transport that depends on stratification and thermal diffusion.

As a summary of the nonlinear dynamics with varying Pr , we display in figures 16(c) and 17 the temporal evolution of the total energy $E(t)$ and instantaneous velocity fields for different Pr at $Re_i = 200$ and $N = 1$. We see in figure 16(c) that, as Pr is small, $Pr < 10^{-4}$, the energy curves collapse and become identical to the curve of the unstratified case with $N = 0$. Instantaneous velocity fields obtained at $t = 500$ from various DNS, which started from the same configuration of the initial condition described in the early part of § 4, are also identical between the stratified cases with $Pr = 10^{-5}$ and 10^{-6} and unstratified case with $N = 0$. These results support the explanation in the introduction and figure 1 that the stratification effect is suppressed by strong thermal diffusion and the flow

behaves as unstratified flow in both linear and nonlinear regimes. Nonetheless, there still remains a question as to whether our conclusion will remain valid for turbulent cases and if so, up to which Reynolds number Re . Although DNS investigations like those by Prat & Lignières (2013) verified this question for Re of $O(100)$, further investigations should be conducted at higher Reynolds numbers.

5. Conclusion and discussion

In this paper, linear and nonlinear dynamics of centrifugal instability of stratified Taylor–Couette flow are studied for diffusive fluids in which the Prandtl number Pr is low, $Pr \leq 1$. The LSA reveals that the stratification effect, which suppresses the centrifugal instability (Boubnov *et al.* 1995; Caton *et al.* 2000), is suppressed by strong thermal diffusion. This implies that the thermal diffusion promotes centrifugal instability of stratified Taylor–Couette flow, a situation which can be found similarly in other contexts like shear instabilities in stratified flows in the low- Pr limit (Lignières 1999; Garaud 2020a). When the thermal diffusion is sufficiently strong, we apply the small- Pr approximation and find that the instability characteristics are self-similar with the new scaled parameter $P_N = N^2 Pr$ (see also Lignières 1999; Park *et al.* 2020). The thermal diffusion effect as promoting centrifugal instability is found to be the same for both axisymmetric and non-axisymmetric perturbations. For the parameters considered here (i.e. $\mu = 0$, $\eta = 0.9$ and $Pr \leq 1$), it is found that the axisymmetric perturbation with $m = 0$ is most unstable compared with non-axisymmetric perturbations. By conducting DNS for the Reynolds number Re_i above the critical one, $Re_i > Re_{i,c}$, we also study the nonlinear evolution of centrifugal instability. In the DNS, we use controlled initial conditions with both the axisymmetric perturbation and a smaller-amplitude non-axisymmetric perturbation to see how they grow and interact nonlinearly and to understand their nonlinear modal interaction leading to different states. At the initial stage, the axisymmetric perturbation grows fastest and saturates along the nonlinear interaction with base flow. Depending on Re_i , a new mean flow in the shape of axisymmetric Taylor vortices can become secondarily unstable by the growth of non-axisymmetric perturbation. Unlike the case of primary instability, which is promoted by strong thermal diffusion, the 2-D bi-global LSA of the Taylor vortices reveals that thermal diffusion in the range $10^{-3} < Pr < 1$ at $N = 1$ delays the onset of secondary instability and potentially laminar–turbulent transition triggered by highly non-axisymmetric perturbations. We note that the appearance of such a non-axisymmetric flow pattern by the onset of secondary instability in highly diffusive and stratified flows has not been explored properly in previous studies. At $Pr = 1$, we also examine irregular flow patterns leading to chaotic mixing of temperature, the state as a precursor to turbulence. Furthermore, we analyse how the Nusselt number Nu as a measure of angular momentum transfer varies with the Reynolds number Re_i for various sets of (N, Pr) . It is verified that the secondary instability slows down the increase of Nu , implying that the momentum transfer is slowly enhanced after the onset of secondary instability.

In recent years, stratified turbulence in the low- Pr regime has been studied increasingly not only in fluid dynamics but also in astrophysics due to its relevance to the interior of stars and the Sun where the Prandtl number Pr is low as 10^{-6} or below (Garaud 2020a; Dymott *et al.* 2023; Garaud *et al.* 2024b). Although the Reynolds numbers of astrophysical flows cannot be reached due to their immensely large length scales, simulations at lower Reynolds numbers and theories unveil new regimes of turbulence and give us a hint as to how stratified turbulence behaves with strong thermal diffusion (Cope *et al.* 2020; Skoutnev 2023; Garaud *et al.* 2024a). What has not been explored yet though in these

turbulence studies is how the turbulence is generated via laminar–turbulent transition processes. In this regard, the current study contributes to our knowledge of how the centrifugal instability develops nonlinearly towards turbulence in stratified and highly diffusive fluids. Beyond this paper, we will aim to study first the characteristics of fully developed stratified-rotating turbulence triggered by centrifugal instability in the low- Pr regime. At low Pr , an unexpected highly non-axisymmetric pattern can generate turbulent flow with characteristics different from those of unstratified turbulence. Another topic to be investigated in the future is how the SRI will behave in the presence of strong thermal diffusion. From the perspective of linear instability, the thermal diffusion suppressing the stratification effect is expected to suppress the SRI as well. Linear and nonlinear SRIs need to be further explored in the low- Pr regime. The nonlinear development of the SRI is also of great interest in geophysical and astrophysical fluid dynamics, in particular for flows in the Keplerian or super-rotation regimes, the latter in which the outer part rotates faster than the inner region (Dubrulle *et al.* 2005; Le Dizès & Riedinger 2010; Park & Billant 2013).

Supplementary movies. Supplementary movies are available at <https://doi.org/10.1017/jfm.2025.261>.

Funding. The author acknowledges support from the Engineering and Physical Sciences Research Council (EPSRC) through the EPSRC mathematical sciences small grant (EP/W019558/1).

Declaration of interests. The author reports no conflict of interest.

Appendix A. Details of vectors and operator matrices

A.1. Vectors and operator matrices for the evolution equation (2.24) and 1-D LSA

For the case with the index $l \neq 0$, we consider in (2.24) the following vectors and matrices:

$$\tilde{\mathbf{q}}_{jl} = \begin{pmatrix} \tilde{u}_{jl} \\ \tilde{v}_{jl} \\ \tilde{T}_{jl} \end{pmatrix}, \quad \tilde{\mathbf{N}}_{jl} = \begin{pmatrix} -\tilde{N}_{r,jl} - \frac{i}{k_l} \frac{\partial \tilde{N}_{z,jl}}{\partial r} \\ -\tilde{N}_{\theta,jl} + \frac{m_j \tilde{N}_{z,jl}}{k_l r} \\ -\tilde{N}_{T,jl} \end{pmatrix}, \quad (\text{A1})$$

$$\mathcal{A}_{jl} = \begin{pmatrix} \mathcal{A}_{jl}^{11} & \mathcal{A}_{jl}^{12} & 0 \\ \mathcal{A}_{jl}^{21} & \mathcal{A}_{jl}^{22} & 0 \\ 0 & 0 & 1 \end{pmatrix}, \quad \mathcal{B}_{jl} = \begin{pmatrix} \mathcal{B}_{jl}^{11} & \mathcal{B}_{jl}^{12} & \mathcal{B}_{jl}^{13} \\ \mathcal{B}_{jl}^{21} & \mathcal{B}_{jl}^{22} & \mathcal{B}_{jl}^{23} \\ \mathcal{B}_{jl}^{31} & \mathcal{B}_{jl}^{32} & \mathcal{B}_{jl}^{33} \end{pmatrix}, \quad (\text{A2})$$

where

$$\begin{aligned} \mathcal{A}_{jl}^{11} &= 1 - \frac{1}{k_l^2} \frac{\partial}{\partial r} \left(\frac{\partial}{\partial r} + \frac{1}{r} \right), \quad \mathcal{A}_{jl}^{12} = -\frac{im_j}{k_l^2 r} \left(\frac{\partial}{\partial r} - \frac{1}{r} \right), \\ \mathcal{A}_{jl}^{21} &= -\frac{im_j}{k_l^2 r} \left(\frac{\partial}{\partial r} + \frac{1}{r} \right), \quad \mathcal{A}_{jl}^{22} = 1 + \frac{m_j^2}{k_l^2 r^2}, \end{aligned} \quad (\text{A3})$$

$$\begin{aligned} \mathcal{B}_{jl}^{11} &= -im_j \Omega + \frac{im_j}{k_l^2} \left(\Omega \frac{\partial}{\partial r} + \frac{d\Omega}{dr} \right) \left(\frac{\partial}{\partial r} + \frac{1}{r} \right) \\ &+ \frac{1}{Re} \left[\tilde{\nabla}_{jl}^2 - \frac{1}{r^2} - \frac{1}{k_l^2} \frac{\partial}{\partial r} \tilde{\nabla}_{jl}^2 \left(\frac{\partial}{\partial r} + \frac{1}{r} \right) \right], \end{aligned}$$

$$\begin{aligned}
 \mathcal{B}_{jl}^{12} &= 2\Omega + \frac{im_j}{k_l^2} \left(\Omega \frac{\partial}{\partial r} + \frac{d\Omega}{dr} \right) \left(\frac{im_j}{r} \right) \\
 &\quad + \frac{1}{Re} \left[-\frac{2im_j}{r^2} - \frac{1}{k_l^2} \frac{\partial}{\partial r} \tilde{\nabla}_{jl}^2 \left(\frac{im_j}{r} \right) \right], \quad \mathcal{B}_{jl}^{13} = \frac{iN^2}{k_l} \frac{\partial}{\partial r}, \\
 \mathcal{B}_{jl}^{21} &= -Z - \frac{m_j^2 \Omega}{k_l^2 r} \left(\frac{\partial}{\partial r} + \frac{1}{r} \right) + \frac{1}{Re} \left[\frac{2im_j}{r^2} - \frac{im_j}{k_l^2 r} \tilde{\nabla}_{jl}^2 \left(\frac{\partial}{\partial r} + \frac{1}{r} \right) \right], \\
 \mathcal{B}_{jl}^{22} &= -im_j \Omega - \frac{im_j^3 \Omega}{k_l^2 r^2} + \frac{1}{Re} \left[\tilde{\nabla}_{jl}^2 - \frac{1}{r^2} + \frac{m_j^2}{k_l^2 r} \tilde{\nabla}_{jl}^2 \left(\frac{1}{r} \right) \right], \quad \mathcal{B}_{jl}^{23} = -\frac{m_j N^2}{k_l r}, \\
 \mathcal{B}_{jl}^{31} &= -\frac{i}{k} \left(\frac{\partial}{\partial r} + \frac{1}{r} \right), \quad \mathcal{B}_{jl}^{32} = \frac{m_j}{k_l r}, \quad \mathcal{B}_{jl}^{33} = -im_j \Omega + \frac{1}{Re Pr} \tilde{\nabla}_{jl}^2. \tag{A4}
 \end{aligned}$$

For the case with $l = 0$ and $j \neq 0$, we consider in (2.24) the following vectors and matrices:

$$\tilde{\mathbf{q}}_{j0} = \begin{pmatrix} \tilde{u}_{j0} \\ \tilde{w}_{j0} \\ \tilde{T}_{j0} \end{pmatrix}, \quad \tilde{\mathbf{N}}_{j0} = \begin{pmatrix} -\tilde{N}_{r,j0} - \frac{i}{m_j} \left(\tilde{N}_{\theta,j0} + r \frac{\partial \tilde{N}_{\theta,j0}}{\partial r} \right) \\ -\tilde{N}_{z,j0} \\ -\tilde{N}_{T,j0} \end{pmatrix}, \tag{A5}$$

$$\mathcal{A}_{j0} = \begin{pmatrix} \mathcal{A}_{j0}^{11} & 0 & 0 \\ 0 & 1 & 0 \\ 0 & 0 & 1 \end{pmatrix}, \quad \mathcal{B}_{j0} = \begin{pmatrix} \mathcal{B}_{j0}^{11} & 0 & 0 \\ 0 & \mathcal{B}_{j0}^{22} & \mathcal{B}_{j0}^{23} \\ 0 & \mathcal{B}_{j0}^{32} & \mathcal{B}_{j0}^{33} \end{pmatrix}, \tag{A6}$$

where

$$\mathcal{A}_{j0}^{11} = 1 - \frac{1}{m_j^2} \left(r^2 \frac{\partial^2}{\partial r^2} + 3r \frac{\partial}{\partial r} + 1 \right), \tag{A7}$$

$$\begin{aligned}
 \mathcal{B}_{j0}^{11} &= \frac{i}{m_j} \left[r^2 \Omega \frac{\partial^2}{\partial r^2} + 3r \Omega \frac{\partial}{\partial r} - r^2 \frac{d^2 \Omega}{dr^2} - 3r \frac{d\Omega}{dr} + (1 - m_j^2) \Omega \right] \\
 &\quad - \frac{1}{Re m_j^2} \left[\frac{\partial}{\partial r} \left(r \tilde{\nabla}_{j0}^2 + r \tilde{\nabla}_{j0}^2 \left(r \frac{\partial}{\partial r} \right) \right) - m_j^2 \tilde{\nabla}_{j0}^2 - \frac{\partial^2}{\partial r^2} - \frac{1}{r} \frac{\partial}{\partial r} + \frac{1 - 3m_j^2}{r^2} \right], \\
 \mathcal{B}_{j0}^{22} &= -im_j \Omega + \frac{1}{Re} \tilde{\nabla}_{j0}^2, \quad \mathcal{B}_{j0}^{23} = N^2, \quad \mathcal{B}_{j0}^{32} = -1, \\
 \mathcal{B}_{j0}^{33} &= -im_j \Omega + \frac{1}{Re Pr} \tilde{\nabla}_{j0}^2. \tag{A8}
 \end{aligned}$$

For the case with $j = l = 0$, we consider in (2.24) the following vectors and matrices:

$$\tilde{\mathbf{q}}_{00} = \begin{pmatrix} \tilde{v}_{00} \\ \tilde{w}_{00} \\ \tilde{T}_{00} \end{pmatrix}, \quad \tilde{\mathbf{N}}_{00} = \begin{pmatrix} -\tilde{N}_{\theta,00} \\ -\tilde{N}_{z,00} \\ -\tilde{N}_{T,00} \end{pmatrix}, \tag{A9}$$

$$\mathcal{A}_{00} = \begin{pmatrix} 1 & 0 & 0 \\ 0 & 1 & 0 \\ 0 & 0 & 1 \end{pmatrix}, \quad \mathcal{B}_{00} = \begin{pmatrix} \frac{1}{Re} \left(\tilde{\nabla}_{00}^2 - \frac{1}{r^2} \right) & 0 & 0 \\ 0 & \frac{1}{Re} \tilde{\nabla}_{00}^2 & N^2 \\ 0 & -1 & \frac{1}{Re Pr} \tilde{\nabla}_{00}^2 \end{pmatrix}. \quad (\text{A10})$$

In the eigenvalue problem (2.27), the eigenfunction $\hat{\mathbf{q}}$ and operator matrices \mathcal{A} and \mathcal{B} are the same as $\tilde{\mathbf{q}}_{11}$, \mathcal{A}_{11} and \mathcal{B}_{11} for given m and k (i.e. $j = l = 1$).

A.2. Operator matrices in the bi-global stability analysis

For the 2-D base state $\bar{\mathbf{Q}}(r, z) = (\bar{U}, \bar{V}, \bar{W}, \bar{T})$, we consider the following linearised perturbation equations:

$$\frac{\partial \bar{u}_r}{\partial r} + \frac{\bar{u}_r}{r} + \frac{1}{r} \frac{\partial \bar{u}_\theta}{\partial \theta} + \frac{\partial \bar{u}_z}{\partial z} = 0, \quad (\text{A11})$$

$$\begin{aligned} & \frac{\partial \bar{u}_r}{\partial t} + \left(\bar{U} \frac{\partial}{\partial r} + \frac{\bar{V}}{r} \frac{\partial}{\partial \theta} + \bar{W} \frac{\partial}{\partial z} + \frac{\partial \bar{U}}{\partial r} \right) \bar{u}_r - \frac{2\bar{V}}{r} \bar{u}_\theta + \frac{\partial \bar{U}}{\partial z} \bar{u}_z \\ &= -\frac{\partial \bar{p}}{\partial r} + \frac{1}{Re} \left[\left(\nabla^2 - \frac{1}{r^2} \right) \bar{u}_r - \frac{2}{r^2} \frac{\partial \bar{u}_\theta}{\partial \theta} \right], \end{aligned} \quad (\text{A12})$$

$$\begin{aligned} & \frac{\partial \bar{u}_\theta}{\partial t} + \left(\frac{\partial \bar{V}}{\partial r} + \frac{\bar{V}}{r} \right) \bar{u}_r + \left(\bar{U} \frac{\partial}{\partial r} + \frac{\bar{V}}{r} \frac{\partial}{\partial \theta} + \bar{W} \frac{\partial}{\partial z} + \frac{\bar{U}}{r} \right) \bar{u}_\theta + \frac{\partial \bar{V}}{\partial z} \bar{u}_z \\ &= -\frac{1}{r} \frac{\partial \bar{p}}{\partial \theta} + \frac{1}{Re} \left[\left(\nabla^2 - \frac{1}{r^2} \right) \bar{u}_\theta + \frac{2}{r^2} \frac{\partial \bar{u}_r}{\partial \theta} \right], \end{aligned} \quad (\text{A13})$$

$$\frac{\partial \bar{u}_z}{\partial t} + \frac{\partial \bar{W}}{\partial r} \bar{u}_r + \left(\bar{U} \frac{\partial}{\partial r} + \frac{\bar{V}}{r} \frac{\partial}{\partial \theta} + \bar{W} \frac{\partial}{\partial z} + \frac{\partial \bar{W}}{\partial z} \right) \bar{u}_z = -\frac{\partial \bar{p}}{\partial z} + N^2 \bar{T} + \frac{1}{Re} \nabla_m^2 \bar{u}_z, \quad (\text{A14})$$

$$\frac{\partial \bar{T}}{\partial t} + \frac{\partial \bar{T}}{\partial r} \bar{u}_r + \left(\frac{\partial \bar{T}}{\partial z} + 1 \right) \bar{u}_z + \left(\bar{U} \frac{\partial}{\partial r} + \frac{\bar{V}}{r} \frac{\partial}{\partial \theta} + \bar{W} \frac{\partial}{\partial z} \right) \bar{T} = \frac{1}{Re Pr} \nabla^2 \bar{T}. \quad (\text{A15})$$

By applying the normal mode (2.29), we obtain the equations in modal form as follows:

$$\frac{\partial \hat{u}_m}{\partial r} + \frac{\hat{u}_m}{r} + \frac{im \hat{v}_m}{r} + \frac{\partial \hat{w}_m}{\partial z} = 0, \quad (\text{A16})$$

$$\begin{aligned} & -i\omega_m \hat{u}_m + \left(\mathcal{L} + \frac{\partial \bar{U}}{\partial r} \right) \hat{u}_m - \frac{2\bar{V}}{r} \hat{v}_m + \frac{\partial \bar{U}}{\partial z} \hat{w}_m = -\frac{\partial \hat{p}_m}{\partial r} \\ & + \frac{1}{Re} \left[\left(\hat{\nabla}_m^2 - \frac{1}{r^2} \right) \hat{u}_m - \frac{2im \hat{v}_m}{r^2} \right], \end{aligned} \quad (\text{A17})$$

$$-i\omega_m \hat{v}_m + \left(\frac{\partial \bar{V}}{\partial r} + \frac{\bar{V}}{r} \right) \hat{u}_m + \left(\mathcal{L} + \frac{\bar{U}}{r} \right) \hat{v}_m + \frac{\partial \bar{V}}{\partial z} \hat{w}_m = -\frac{im \hat{p}_m}{r} + \frac{1}{Re} \left[\left(\hat{\nabla}_m^2 - \frac{1}{r^2} \right) \hat{v}_m + \frac{2im \hat{u}_m}{r^2} \right], \quad (\text{A18})$$

$$-i\omega_m \hat{w}_m + \frac{\partial \bar{W}}{\partial r} \hat{u}_m + \left(\mathcal{L} + \frac{\partial \bar{W}}{\partial z} \right) \hat{w}_m = -\frac{\partial \hat{p}_m}{\partial z} + N^2 \hat{T}_m + \frac{1}{Re} \hat{\nabla}_m^2 \hat{w}_m, \quad (\text{A19})$$

$$-i\omega_m \hat{T}_m + \frac{\partial \bar{T}}{\partial r} \hat{u}_m + \left(\frac{\partial \bar{T}}{\partial z} + 1 \right) \hat{w}_m + \mathcal{L} \hat{T}_m = \frac{1}{RePr} \hat{\nabla}_m^2 \hat{T}_m, \quad (\text{A20})$$

where $\mathcal{L} = \bar{U}(\partial/\partial r) + im\bar{V}/r + \bar{W}(\partial/\partial z)$ is the advection operator and $\hat{\nabla}_m^2 = \partial^2/\partial r^2 + (1/r)(\partial/\partial r) + m^2/r^2 + \partial^2/\partial z^2$ is the modal Laplacian operator. After eliminating the pressure \hat{p}_m , the above equations can be simplified as the eigenvalue problem (2.30) where the operator matrices \mathcal{A}_m and \mathcal{B}_m are defined as

$$\mathcal{A}_m = \begin{bmatrix} \mathcal{A}_{11,m} & \mathcal{A}_{12,m} & 0 \\ \mathcal{A}_{21,m} & \mathcal{A}_{22,m} & 0 \\ 0 & 0 & 1 \end{bmatrix}, \quad \mathcal{B}_m = \begin{bmatrix} \mathcal{B}_{11,m} & \mathcal{B}_{12,m} & 0 \\ \mathcal{B}_{21,m} & \mathcal{B}_{22,m} & N^2 \\ -\frac{\partial \bar{T}}{\partial r} & -1 - \frac{\partial \bar{T}}{\partial z} & -\mathcal{L} + \frac{\hat{\nabla}_m^2}{RePr} \end{bmatrix}, \quad (\text{A21})$$

where

$$\begin{aligned} \mathcal{A}_{11,m} &= 1 - \frac{1}{m^2} \frac{\partial}{\partial r} \left(r + r^2 \frac{\partial}{\partial r} \right), & \mathcal{A}_{12,m} &= -\frac{1}{m^2} \frac{\partial}{\partial r} \left(r^2 \frac{\partial}{\partial z} \right), \\ \mathcal{A}_{21,m} &= -\frac{1}{m^2} \frac{\partial}{\partial z} \left(r + r^2 \frac{\partial}{\partial r} \right), & \mathcal{A}_{22,m} &= 1 - \frac{1}{m^2} \frac{\partial}{\partial z} \left(r^2 \frac{\partial}{\partial z} \right), \end{aligned} \quad (\text{A22})$$

$$\begin{aligned} \mathcal{B}_{11,m} &= -\mathcal{L} - \frac{\partial \bar{U}}{\partial r} + \frac{1}{Re} \left(\hat{\nabla}_m^2 + \frac{1}{r^2} + \frac{2}{r} \frac{\partial}{\partial r} \right) + \frac{2i}{m} \left(\frac{\bar{V}}{r} + \bar{V} \frac{\partial}{\partial r} \right) \\ &\quad + \frac{1}{m^2} \frac{\partial}{\partial r} \left[\left(r\mathcal{L} + \bar{U} - \frac{r\hat{\nabla}_m^2}{Re} + \frac{1}{Re r} \right) \left(1 + r \frac{\partial}{\partial r} \right) \right] \\ &\quad - \frac{i}{m} \frac{\partial}{\partial r} \left(\bar{V} + r \frac{\partial \bar{V}}{\partial r} - \frac{2im}{Re r} \right), \\ \mathcal{B}_{12,m} &= \frac{i}{m} \left[2\bar{V} \frac{\partial}{\partial z} - \frac{\partial}{\partial r} \left(r \frac{\partial \bar{V}}{\partial z} \right) \right] - \frac{\partial \bar{U}}{\partial z} + \frac{2}{Re r} \frac{\partial}{\partial z} \\ &\quad + \frac{1}{m^2} \frac{\partial}{\partial r} \left[\left(r\mathcal{L} + \bar{U} - \frac{r\hat{\nabla}_m^2}{Re} + \frac{1}{Re r} \right) \left(r \frac{\partial}{\partial z} \right) \right], \\ \mathcal{B}_{21,m} &= -\frac{\partial \bar{W}}{\partial r} + \frac{1}{m^2} \frac{\partial}{\partial z} \left[\left(r\mathcal{L} + \bar{U} - \frac{r\hat{\nabla}_m^2}{Re} + \frac{1}{Re r} \right) \left(1 + r \frac{\partial}{\partial r} \right) \right] \\ &\quad - \frac{i}{m} \frac{\partial}{\partial z} \left(\bar{V} + r \frac{\partial \bar{V}}{\partial r} - \frac{2im}{Re r} \right), \end{aligned}$$

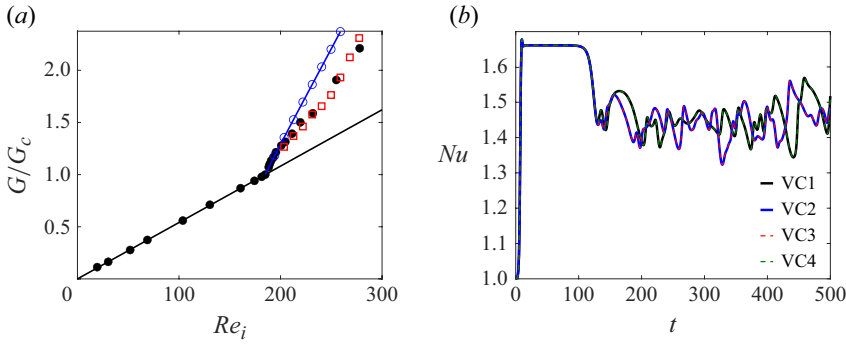


Figure 18. (a) Normalised torque G/G_c at the inner cylinder versus the Reynolds number Re_i for an unstratified case $N=0$ at $\mu=0$ and $\eta=0.95$. Results are from the laminar solution (black solid line), experiments (black filled circles) from Donnelly & Simon (1960), axisymmetric 2-D DNS (blue line with open circles) and non-axisymmetric 3-D DNS (red open squares). (b) The Nusselt number Nu versus time t for different VCs.

$$\begin{aligned} \mathcal{B}_{22,m} = & -\mathcal{L} - \frac{\partial \bar{W}}{\partial z} + \frac{\hat{\nabla}_m^2}{Re} + \frac{1}{m^2} \frac{\partial}{\partial z} \left[\left(r\mathcal{L} + \bar{U} - \frac{r\hat{\nabla}_m^2}{Re} + \frac{1}{Rer} \right) \left(r \frac{\partial}{\partial z} \right) \right] \\ & - \frac{i}{m} \frac{\partial}{\partial z} \left(r \frac{\partial \bar{V}}{\partial z} \right). \end{aligned} \quad (\text{A23})$$

Appendix B. Validation

B.1. Validation against experiments

To validate the current DNS code, 2-D and 3-D DNS are conducted for unstratified cases with $N=0$, $\mu=0$ and $\eta=0.95$. The DNS results are compared with experimental results from Donnelly & Simon (1960), which details an empirical relation for the torque measured at the inner cylinder. In this case, the critical Reynolds number is $Re_{i,c} = 185$ for the axisymmetric mode with $k_d = 3.128$ (according to DiPrima *et al.* (1984) as well as our 1-D LSA computation). We conduct two types of DNS: an axisymmetric 2-D DNS by considering only the axisymmetric modes with $m=0$ (e.g. $M=0$ and $N_\theta=1$ in the DNS) and a non-axisymmetric 3-D DNS by considering both axisymmetric and non-axisymmetric modes. For both DNS, one periodic length $\lambda_z = 2\pi/k$ is considered as the axial domain length. At each Re_i , the most unstable axisymmetric mode with $k_d = 3.128$ with its modal energy $\tilde{E}_{01} = 5 \times 10^{-7}$ is considered as an initial condition in the axisymmetric DNS. In the non-axisymmetric DNS, a non-axisymmetric mode with $(m, k_d) = (1, 3.128)$ with a smaller energy $\tilde{E}_{11} = 5 \times 10^{-9}$ is added to the initial condition. From experiments, Donnelly & Simon (1960) present the relation between the torque and the Reynolds number Re_i . In figure 18(a), we plot the non-dimensional torque G normalised by the torque G_c at the critical Reynolds number $Re_{i,c} = 185$ to facilitate the comparison between their experiments and our DNS. In the range $1 < \mathcal{R}_c < 1.1$ (i.e. $185 < Re_i < 203.5$), the axisymmetric DNS demonstrating the saturation of centrifugal instability with axisymmetric Taylor vortices agree well the experimental results for the torque. For $\mathcal{R}_c > 1.1$ (i.e. $Re_i > 203.5$), non-axisymmetric modes also develop and generate more complex interaction between modes and base state, leading to a new saturated state in oscillatory motion known as wavy Taylor vortices. This explains the torque difference between the axisymmetric 2-D and non-axisymmetric 3-D DNS cases.

Case	N_r	N_θ	N_z	L_z
VC1	60	33	33	$2\pi/k$
VC2	120	65	65	$2\pi/k$
VC3	120	65	129	$4\pi/k$
VC4	60	33	129	$8\pi/k$

Table 4. Numerical parameters for different VCs at $Re_i = 200$, $N = 1$, $Pr = 1$, $k = 30.6$.

As shown in [figure 18\(a\)](#), the torque measured from experiments agrees well with the prediction from the DNS.

B.2. Validation of numerical resolution and domain size

For case 3 with $(Re_i, N, Pr) = (200, 1, 1)$, which is the case where the flow becomes chaotic, different numerical resolutions and domain sizes are tested as detailed in [table 4](#) where validation case (VC) 2 is the same as case 3 and other VCs have lower resolutions or longer domain lengths than VC2. As shown in [figure 18\(b\)](#), the Nusselt number Nu , which is an averaged quantity over the axial domain length, is the same for every case at saturation and before the flow becomes chaotic. The fluctuation behaviour of Nu is the same for VC1 and VC4 (low-resolution cases) and for VC2 and VC3 (high-resolution cases). This implies that the choice of the axial domain size as one periodic axial length is validated for case 3. Although the fluctuation is different between low- and high-resolution cases, their time-averaged Nu do not vary significantly; thus the mean Nusselt numbers like those in [figure 16](#) may vary insignificantly with resolutions. This aspect should, however, be further validated if the flow becomes fully turbulent at higher Reynolds numbers.

REFERENCES

- ABRAMOWITZ, M. & STEGUN, I. 1965 *Handbook of Mathematical Functions*. Dover.
- ANTKOWIAK, A. & BRANCHER, P. 2004 Transient energy growth for the Lamb-Oseen vortex. *Phys. Fluids* **16** (1), L1–L4.
- BARKER, A., JONES, C.A. & TOBIAS, S.M. 2019 Angular momentum transport by the GSF instability: non-linear simulations at the equator. *Mon. Not. R. Astron. Soc.* **487** (2), 1777–1794.
- BARKER, A., JONES, C.A. & TOBIAS, S.M. 2020 Angular momentum transport, layering, and zonal jet formation by the GSF instability: non-linear simulations at a general latitude. *Mon. Not. R. Astron. Soc.* **495** (1), 1468–1490.
- BILLANT, P. & GALLAIRE, F. 2005 Generalized Rayleigh criterion for non-axisymmetric centrifugal instabilities. *J. Fluid Mech.* **542**, 365–379.
- BOUBNOV, B.M., GLEDZER, E.B. & HOPFINGER, E.J. 1995 Stratified circular Couette flow: instability and flow regimes. *J. Fluid Mech.* **292**, 333–358.
- CALKINS, M.A., AURNOU, J.M., ELDRIDGE, J.D. & JULIEN, K. 2012 The influence of fluid properties on the morphology of core turbulence and the geomagnetic field. *Earth Planet. Sci. Lett.* **359–360**, 55–60.
- CATON, F., JANIAUD, B. & HOPFINGER, E.J. 2000 Stability and bifurcations in stratified Taylor–Couette flow. *J. Fluid. Mech.* **419**, 93–124.
- CHANG, E. & GARAUD, P. 2021 Modelling coexisting GSF and shear instabilities in rotating stars. *Mon. Not. R. Astron. Soc.* **506** (4), 4914–4932.
- COPE, L., GARAUD, P. & CAULFIELD, C.P. 2020 The dynamics of stratified horizontal shear flows at low Péclet number. *J. Fluid Mech.* **903**, A1.
- DAVEY, A., DIPRIMA, R.C. & STUART, J.T. 1968 On the instability of Taylor vortices. *J. Fluid. Mech.* **31** (1), 17–52.
- DELONCLE, A., BILLANT, P. & CHOMAZ, J.-M. 2008 Nonlinear evolution of the zigzag instability in stratified fluids: a shortcut on the route to dissipation. *J. Fluid Mech.* **599**, 229–239.
- DIPRIMA, R.C., EAGLES, P.M. & NG, B.S. 1984 The effect of radius ratio on the stability of Couette flow and Taylor vortex flow. *Phys. Fluids* **27** (10), 2403–2411.

- DONNELLY, R.J. & SIMON, N.J. 1960 An empirical torque relation for supercritical flow between rotating cylinders. *J. Fluid. Mech.* **7** (3), 401–418.
- DUBRULLE, B., DAUCHOT, O., DAVIAUD, F., LONGARETTI, P.-Y. & ZAHN, J.-P. 2005 Stability and turbulent transport in Taylor–Couette flow from analysis of experimental data. *Phys. Fluids* **17** (9), 095103.
- DUBRULLE, B. & HERSANT, F. 2002 Momentum transport and torque scaling in Taylor–Couette flow from an analogy with turbulent convection. *Eur. Phys. J. B* **26** (3), 379–386.
- DYMOTT, R.W., BARKER, A., JONES, C.A. & TOBIAS, S.M. 2023 Linear and non-linear properties of the Goldreich–Schubert–Fricke instability in stellar interiors with arbitrary local radial and latitudinal differential rotation. *Mon. Not. R. Astron. Soc.* **524** (2), 2857–2882.
- EAGLES, P.M. 1974 On the torque of wavy vortices. *J. Fluid. Mech.* **62** (1), 1–9.
- ECKHARDT, B., GROSSMANN, S. & LOHSE, D. 2007 Torque scaling in turbulent Taylor–Couette flow between independently rotating cylinders. *J. Fluid. Mech.* **581**, 221–250.
- GARAUD, P. 2020*a* Horizontal shear instabilities at low Prandtl number. *Astrophys. J.* **901** (2), 146.
- GARAUD, P. 2020*b* The tachocline revisited. In *Dynamics of the Sun and Stars* (eds. R.A. Mário J.P.F.G. Monteiro, J.C.-D. García & M. Scott W.), pp. 207–220. Springer International Publishing.
- GARAUD, P., CHINI, G.P., COPE, L., SHAH, K. & CAULFIELD, C.P. 2024*a* Numerical validation of scaling laws for stratified turbulence. *J. Fluid. Mech.* **991**, R1.
- GARAUD, P., KHAN, S. & BROWN, J. 2024*b* The combined effects of vertical and horizontal shear instabilities in stellar radiative zones. *Astrophys. J.* **961** (2), 220.
- GUSEVA, A., WILLIS, A.P., HOLLERBACH, R. & AVILA, M. 2015 Transition to magnetorotational turbulence in Taylor–Couette flow with imposed azimuthal magnetic field. *New J. Phys.* **17** (9), 093018.
- HORN, S., SHISHKINA, O. & WAGNER, C. 2013 On non-Oberbeck-Boussinesq effects in three-dimensional Rayleigh–Bénard convection in glycerol. *J. Fluid. Mech.* **724**, 175–202.
- IBANEZ, R., SWINNEY, H.L. & RODENBORN, B. 2016 Observations of the stratorotational instability in rotating concentric cylinders. *Phys. Rev. Fluids* **1** (5), 053601.
- KERR, R.M. & HERRING, J.R. 2000 Prandtl number dependence of Nusselt number in direct numerical simulations. *J. Fluid Mech.* **419**, 325–344.
- KIM, J., MOIN, P. & MOSER, R. 1987 Turbulence statistics in fully developed channel flow at low Reynolds number. *J. Fluid Mech.* **177**, 133–166.
- LANGHAM, J., EAVES, T.S. & KERSWELL, R.R. 2020 Stably stratified exact coherent structures in shear flow: the effect of Prandtl number. *J. Fluid Mech.* **882**, A10.
- LE BARS, M. & LE GAL, P. 2007 Experimental analysis of the stratorotational instability in a cylindrical Couette flow. *Phys. Rev. Lett.* **99** (6), 064502.
- LE DIZÈS, S. & RIEDINGER, X. 2010 The strato-rotational instability of Taylor–Couette and Keplerian flows. *J. Fluid Mech.* **660**, 147–161.
- LECLERCQ, C., NGUYEN, F. & KERSWELL, R.R. 2016 Connections between centrifugal, stratorotational, and radiative instabilities in viscous Taylor–Couette flow. *Phys. Rev. E* **94** (4), 043103.
- LEGASPI, J.D. & WAITE, M.L. 2020 Prandtl number dependence of stratified turbulence. *J. Fluid. Mech.* **903**, A12.
- LIGNIÈRES, F. 1999 The small-Péclet-number approximation in stellar radiation zones. *Astron. Astrophys.* **348**, 933–939.
- LIGNIÈRES, F., CALIFANO, F. & MANGENEY, A. 1999 Shear layer instability in a highly diffusive stably stratified atmosphere. *Astron. Astrophys.* **349**, 1027–1036.
- LÓPEZ, J.M., FELDMANN, D., RAMPP, M., VELA-MARTÍN, A., SHI, L. & AVILA, M. 2020 nsCouette – a high-performance code for direct numerical simulations of turbulent Taylor–Couette flow. *SoftwareX* **11**, 100395.
- LOPEZ, J.M. & MARQUES, F. 2020 Impact of centrifugal buoyancy on strato-rotational instability. *J. Fluid Mech.* **890**, A9.
- LOPEZ, J.M. & MARQUES, F. 2022 Stratified Taylor–Couette flow: nonlinear dynamics. *J. Fluid Mech.* **930**, A2.
- MARTÍNEZ ARIAS, B. 2015 Torque measurement in turbulent Couette-Taylor flows. PhD thesis, Université du Havre.
- MATHIS, S., PRAT, V., AMARD, L., CHARBONNEL, C., PALACIOS, A., LAGARDE, N. & EGGENBERGER, P. 2018 Anisotropic turbulent transport in stably stratified rotating stellar radiation zones. *Astron. Astrophys.* **620**, A22.
- MELETTI, G., ABIDE, S., VIAZZO, S., KREBS, A. & HARLANDER, U. 2021 Experiments and long-term high-performance computations on amplitude modulations of strato-rotational flows. *Geophys. Astrophys. Fluid Dyn.* **115** (3), 297–321.
- MEYER, K.A. 1966 A two-dimensional time-dependent numerical study of rotational Couette flow. Tech. Rep. Los Alamos Scientific Laboratory.

- MIQUEL, B., BOUILLAUT, V., AUMAÎTRE, S. & GALLET, B. 2020 On the role of the Prandtl number in convection driven by heat sources and sinks. *J. Fluid Mech.* **900**, R1.
- MOLEMAKER, M.J., MCWILLIAMS, J. & YAVNEH, I. 2001 Instability and equilibration of centrifugally stable stratified Taylor–Couette flow. *Phys. Rev. Lett.* **86** (23), 5270–5273.
- ORR, W.M.F. 1907 The stability or instability of the steady motions of a perfect liquid and of a viscous liquid. Part II: a viscous liquid. *Proc. R. Irish Acad. A* **27**, 69–138.
- PARK, J. 2012 Waves and instabilities on vortices in stratified and rotating fluids. PhD thesis, Ecole Polytechnique.
- PARK, J. & BILLANT, P. 2013 The stably stratified Taylor–Couette flow is always unstable except for solid-body rotation. *J. Fluid Mech.* **725**, 262–280.
- PARK, J., BILLANT, P. & BAIK, J.-J. 2017 Instabilities and transient growth of the stratified Taylor–Couette flow in a Rayleigh-unstable regime. *J. Fluid Mech.* **822**, 80–108.
- PARK, J., BILLANT, P., BAIK, J.-J. & SEO, J.M. 2018 Competition between the centrifugal and stratorotational instabilities in the stratified Taylor–Couette flow. *J. Fluid Mech.* **840**, 5–24.
- PARK, J., HWANG, Y. & COSSU, C. 2011 On the stability of large-scale streaks in turbulent Couette and Poiseuille flows. *Comptes Rendus. Mécanique* **339** (1), 1–5.
- PARK, J., MOON, S., SEO, J.M. & BAIK, J.-J. 2021a Systematic comparison between the generalized Lorenz equations and DNS in the two-dimensional Rayleigh–Bénard convection. *Chaos* **31** (7), 073119.
- PARK, J., PRAT, V. & MATHIS, S. 2020 Horizontal shear instabilities in rotating stellar radiation zones. I. Inflectional and inertial instabilities and the effects of thermal diffusion. *Astron. Astrophys.* **635**, A133.
- PARK, J., PRAT, V. & MATHIS, S. 2021b Horizontal shear instabilities in rotating stellar radiation zones. II. Effects of the full Coriolis acceleration. *Astron. Astrophys.* A64.
- PRAT, V. & LIGNIÈRES, F. 2013 Turbulent transport in radiation zones of stars. *Astron. Astrophys.* **551**, L3.
- PRAT, V. & LIGNIÈRES, F. 2014 Shear mixing in stellar radiative zones. I. Effect of thermal diffusion and chemical stratification. *Astron. Astrophys.* **566**, A110.
- PRAT, V. & MATHIS, S. 2021 Anisotropic turbulent transport with horizontal shear in stellar radiative zones. *Astron. Astrophys.* **649**, A62.
- RICHARD, D. & ZAHN, J.-P. 1999 Turbulence in differentially rotating flows. What can be learned from the Couette–Taylor experiment. *Astron. Astrophys.* **347**, 734–738.
- ROBINS, L.J.M., KERSALÉ, E. & JONES, C.A. 2020 Viscous and inviscid strato-rotational instability. *J. Fluid Mech.* **894**, A13.
- RÜDIGER, G., SEELIG, T., SCHULTZ, M., GELLERT, M., EGBERS, CH & HARLANDER, U. 2017 The stratorotational instability of Taylor–Couette flows with moderate Reynolds numbers. *Geophys. Astrophys. Fluid Dyn.* **111** (6), 429–447.
- RÜDIGER, G. & SHALYBKOV, D.A. 2009 Stratorotational instability in MHD Taylor–Couette flows. *Astron. Astrophys.* **493** (2), 375–383.
- SALTZMAN, B. 1962 Finite amplitude free convection as an initial value problem – I. *J. Atmos. Sci.* **19** (4), 329–341.
- SEELIG, T., HARLANDER, U. & GELLERT, M. 2018 Experimental investigation of stratorotational instability using a thermally stratified system: instability, waves and associated momentum flux. *Geophys. Astrophys. Fluid Dyn.* **112** (4), 239–264.
- SKOUTNEV, V.A. 2023 Critical balance and scaling of strongly stratified turbulence at low Prandtl number. *J. Fluid Mech.* **956**, A7.
- STEWART, G.W. 2002 A Krylov–Schur algorithm for large eigenproblems. *SIAM J. Matrix Anal. Appl.* **23** (3), 601–614.
- WANG, C. & BALMFORTH, N.J. 2018 Strato-rotational instability without resonance. *J. Fluid Mech.* **846**, 815–833.
- WITHJACK, E.M. & CHEN, C.F. 1975 Stability analysis of rotational Couette flow of stratified fluids. *J. Fluid Mech.* **68** (01), 157–175.
- YAVNEH, I., MCWILLIAMS, J. & MOLEMAKER, M.J. 2001 Non-axisymmetric instability of centrifugally stable stratified Taylor–Couette flow. *J. Fluid Mech.* **448**, 1–21.
- YIM, E., BILLANT, P. & GALLAIRE, F. 2020 Nonlinear evolution of the centrifugal instability using a semilinear model. *J. Fluid Mech.* **897**, A34.
- YIM, E., BILLANT, P. & GALLAIRE, F. 2023 Weakly nonlinear versus semi-linear models of the nonlinear evolution of the centrifugal instability. *J. Fluid Mech.* **957**, A18.
- YIM, E., BILLANT, P. & MÉNESGUEN, C. 2016 Stability of an isolated pancake vortex in continuously stratified-rotating fluids. *J. Fluid Mech.* **801**, 508–553.
- ZAHN, J.-P. 1992 Circulation and turbulence in rotating stars. *Astron. Astrophys.* **265**, 115–132.